Journal of Hydrology 560 (2018) 202–219

Contents lists available at ScienceDirect

Journal of Hydrology

journal homepage: www.elsevier.com/locate/jhydrol

Research papers

Optimal Interpolation scheme to generate reference crop evapotranspiration

Miquel Tomas-Burguera [a,*], Santiago Beguería [a], Sergio Vicente-Serrano [b], Marco Maneta [c]

[a] Estación Experimental de Aula Dei, Consejo Superior de Investigaciones Cientiíficas (EEAD-CSIC), Avda. Montañana 1005, Zaragoza E-50059, Spain
[b] Instituto Pirenaico de Ecologia, Consejo Superior de Investigaciones Científicas (IPE-CSIC), Avda. Montañana 1005, Zaragoza E-50059, Spain
[c] Department of Geosciences, University of Montana, Missoula, Montana, USA

ARTICLE INFO

Article history:
Received 2 October 2017
Received in revised form 7 March 2018
Accepted 9 March 2018
Available online 13 March 2018
This manuscript was handled by A. Bardossy, Editor-in-Chief, with the assistance of Uwe Haberlandt, Associate Editor

Keywords:
Reference crop evapotranspiration database
Optimal Interpolation
Uncertainty estimation
Regional Climate Model
Weather stations

ABSTRACT

We used an Optimal Interpolation (OI) scheme to generate a reference crop evapotranspiration (ET_o) grid, forcing meteorological variables, and their respective error variance in the Iberian Peninsula for the period 1989–2011. To perform the OI we used observational data from the Spanish Meteorological Agency (AEMET) and outputs from a physically-based climate model. To compute ET_o we used five OI schemes to generate grids for the five observed climate variables necessary to compute ET_o using the FAO-recommended form of the Penman-Monteith equation (FAO-PM). The granularity of the resulting grids are less sensitive to variations in the density and distribution of the observational network than those generated by other interpolation methods. This is because our implementation of the OI method uses a physically-based climate model as prior background information about the spatial distribution of the climatic variables, which is critical for under-observed regions. This provides temporal consistency in the spatial variability of the climatic fields. We also show that increases in the density and improvements in the distribution of the observational network reduces substantially the uncertainty of the climatic and ET_o estimates. Finally, a sensitivity analysis of observational uncertainties and network densification suggests the existence of a trade-off between quantity and quality of observations.

1. Introduction

Estimations of the atmospheric evaporative demand (AED) are critical for understanding and diagnosing imbalances in the hydrologic supply and demand systems of a region. Of the available methods to estimate AED, the Food and Agriculture Organization recommended form of the Penman-Monteith equation (FAO-PM ET_o) is considered the best and most reliable one. The FAO-PM is a modification of the physically-based Penman-Monteith equation proposed in the FAO-56 manual (Allen et al., 1998), and has been shown to outperform other methods under a wide range of conditions. However, this method is data intensive, requiring information on air temperature, relative humidity, solar radiation, and wind speed. Simultaneous information on all these variables is often unavailable at monitored locations used for regional AED analysis.

Alternatives to obtain ET_o estimates using less data-demanding models exist, often only requiring information on air temperature (e.g. Blaney and Criddle, 1950;Priestley and Taylor, 1972; Hargreaves and Samani, 1985). However, as Irmak et al. (2012) and McVicar et al. (2012) pointed out, the information carried by the additional meteorological variables required by the FAO-PM method are critical to obtain reliable ET_o estimates. Hence, it is important to find a methodology that permits the generalization of the FAO-PM calculations to locations for which full information on meteorological conditions is not available. A first attempt at this generalization was included in the FAO-56 manual (Allen et al., 1998), recommending a methodology to estimate missing data using stationary relationships between temperature and other variables. This method, hereinafter referred to as FAO-PMT, is however not devoid of problems due to the assumption of stationarity in the relationship between meteorological variables.

An alternative approach consists in using spatial interpolation to estimate the value of missing variables at the desired locations using data from nearby stations, an option that Tomas-Burguera et al. (2017) showed to perform better than FAO-PMT or other simplified models such as Hargreaves and Samani, at least in the Iberian Peninsula (IP). This methodology have been tested in other regions, such as Greece (Mardikis et al., 2005), China (McVicar et al., 2007), Austria (Haslinger and Bartsch, 2016), or Great Britain

* Corresponding author.
E-mail address: mtomas@eead.csic.es (M. Tomas-Burguera).

https://doi.org/10.1016/j.jhydrol.2018.03.025
0022-1694/

(Robinson et al., 2017). The last two efforts resulted in the development of high spatial resolution (1 km) datasets for these countries.

Also in Britain, Prudhomme and Williamson (2013) tested the use of HadRM3-Q0 to quantify potential evapotranspiration and compared it against the Meteorological Office Rainfall and Evaporation Calculation System (MORECS) observational grid. In the Conterminous United States, Abatzoglou (2013) constructed a FAO-PM-based ET_o dataset derived from his 4 km resolution daily downscaling of meteorological variables. At a much coarser spatial resolution, the Climate Research Unit (CRU) TS dataset also offers an estimation of the FAO-PM ET_o with global coverage (Harris et al., 2014).

While gridded datasets based on spatial interpolation methods are easy to implement, the quality of the results is highly dependent on the spatial density of the observational dataset used for interpolation. The minimum necessary density of the observational network capable of resolving the meteorological field depends on the spatial variability of the meteorological variable, and smoothing of the meteorological field occurs when the observational network is sparse. This smoothing is exacerbated in regions of complex terrain (Silverman and Maneta, 2016). Moreover, geostatistical interpolation methods often rest on the assumption that the spatial model (the semivariogram) is spatially stationary, an assumption that is not valid in many practical situations, and specially over rugged regions with sparse observational coverage.

The use of climate grids derived from physically-based climate models is an alternative that overcome some of the problems of interpolation methods. These models, which are commonly used in climatological and meteorological studies, have several main advantages: the computed meteorological grids have homogeneous and consistent temporal and spatial coverage, they capture the dependence (covariance) between climatic variables, and they maintain the physical spatial coherence of the field, taking into account the influence of topography on the meteorological variables and reducing the spatial smoothing that is characteristic of classic interpolation methods. There are many examples of the use of meteorological outputs from climatologic models to calculate AED. Ishak et al. (2010) used NCAR/Penn State Mesoscale Model Version 5 (MM5) to downscale ERA-40 (European Centre for Medium-Range Weather Forecasts Re-analysis) (Uppala et al., 2005) for estimating ET_o in a catchment of southwest England. Similarly, Srivastava et al. (2013) compared the performance of ERA-INTERIM (Dee et al., 2011) and National Centers for Environmental Prediction (NCEP)/National Center for Atmospheric Research (NCAR) (Kalnay et al., 1996) reanalysis data downscaled through the Weather Research and Forecasting model (WRF) to estimate ET_o. Strong et al. (2017) tested the use of WRF to estimate ET_o in Utah, comparing the results against the Gridded Evapotranspiration estimation (GridET) framework (Lewis and Allen, 2016) and obtaining a good performance. Despite its advantages, the use of physically-based climate models data to estimate ET_o also presents important issues. The presence of a bias is very common, which is the reason why a bias correction step using ground weather station data is compulsory in forecasting models. Also, most climatologic model products have a coarse resolution and some variables, such as wind speed, are often poorly estimated or carry high uncertainties.

A third alternative is to use a mixture of distinct sources of data for estimating ET_o. For instance, Hart et al. (2009) developed a system to estimate ET_o in California by using weather station data and satellite-based estimates of radiation. Martins et al. (2017) used meteorological fields from a reanalysis at 0.5° of spatial resolution to estimate ET_o, but without the bias correction process conducted by Sheffield et al. (2006) on this dataset.

The different studies described above use the FAO-PM approach to generate ET_o estimates, but do not provide a formal quantification of their uncertainty. Studies that take into account the uncertainty of ET_o estimations look at it mostly as the variation in an ensemble of models (Kay and Davies, 2008;Kingston et al., 2009; Hosseinzadehtalaei et al., 2016), and do not consider the uncertainty of individual members of the ensemble. Unfortunately, the variance of a model ensemble reflects the uncertainty associated with a (finite) set of model architectures, and does not necessarily reflect the quality of each ensemble member, which is critical to interpret patterns emerging form the analysis of individual grids. For instance, Brohan et al. (2006) and Morice et al. (2012) proposed and evaluated distinct methodologies to quantify the uncertainty in the HadCRUT3 and HadCRUT4 datasets, and used this information to evaluate the statistical significance of temporal trends analysis done on these datasets, which allowed them to eliminate non-significant trends from further analysis and interpretation.

The quantification of the uncertainty around interpolated climatologic estimates is specially important when interpolation is based on an inhomogeneous or time-changing network of observations. Variations over time in the uncertainty of the reconstructed climatologic field reflects variations in the quality of the observational network. For instance, changes in the number or location of stations in the network can have important effects on the spatial variance of an interpolated grid. An analysis of the variance in a time series of these grids may yield trends easily attributable to a climate processes if information on the uncertainty of the estimates is not available. Beguería et al. (2016) argued that this may be one of the most important handicaps of the application of spatial interpolation techniques for climatologic studies.

Densifications and reorganizations of regional climatologic networks are very common. For example, the deployment of automatic weather stations in Spain accelerated dramatically during the last decade, increasing the availability of data for the estimation of ET_o. A few decades back, only weather stations from the principal network (approximately 100) measured the variables required to compute ET_o (Azorin-Molina et al., 2015), while currently more than 700 weather stations are collecting and providing near real time data on these variables. Since the spatial distribution of AED is a quantity difficult to measure directly, studies seeking to identify spatial-temporal trends in AED will rely on ET_o grids reconstructed using the FAO-PMT approximation, which in turn relies on information from weather stations. Minimizing and controlling the impact of the configuration of the observational network on the resulting grid is important to avoid miss-interpreting statistical artifacts as a real climatologic process.

Beyond the increasing availability of observational data for climatologic studies, climatologic fields from new physically-based climate models at high spatial resolution have become available thanks to international projects like Coordinated Regional climate Downscaling Experiment (CORDEX) (Giorgi et al., 2009). These models often cover a period starting in 1979 similar to the ERA-INTERIM reanalysis product (Dee et al., 2011). The advantage of these products is that they reconstruct climatological fields that are based on atmospheric physics and largely independent from ground observations, which overcomes some of the disadvantages of interpolated grids.

Unprecedented data availability and access to computational power facilitate the use of data fusion techniques to obtain improved estimates of ET_o. Here we propose to use data assimilation methods to combine information from ground observatories and from physically-based climate models to produce improved climatic and ET_o grids. The variance of the resulting grids is less sensitive to the number of available stations in the observational network, while ensuring that the grid from climate models are conditioned by actual observations. In addition, an estimation of their mean error is also provided as a natural by-product of the method.

Specifically, our methodology is based on Optimal Interpolation (OI), which has been extensively used in the analysis of weather forecasts, in climatology and in oceanography (e.g. Reynolds et al., 2002; Ruiz-Arias et al., 2015; Lusana, 2017). OI is a minimum variance estimator that is easy to implement and that takes into account observational and model uncertainties in the final estimates.

The objective of this paper is to describe the generation of a grid of ET_o over the IP. This grid maximizes the use of all available data while controlling the uncertainty and statistical stability of the resulting grid. To achieve this, we first used ground observations and a Regional Climate Model within an OI scheme to generate gridded estimates and standard errors of each individual meteorological input variable needed to calculate the FAO-PM ET_o. Then we used this information with the FAO-PM equation to obtain the optimal ET_o estimate. To quantify the uncertainty of the gridded ET_o, the errors from each individual gridded input variable were propagated through the FAO-PM equation using a first order method. We then analyzed the resulting grids to assess if it reduces some of the problems detected in standard interpolation methods such as kriging.

2. Dataset

Daily meteorological data on maximum (T_{max}) and minimum temperature (T_{min}), relative humidity (RH), wind speed (W) and sunshine duration (SD) (as the best available surrogate for solar radiation, which is poorly measured in Spain, (Sanchez-Lorenzo et al., 2013)) from 1989 to 2011 was provided by the Spanish meteorological agency (AEMET). A quality control process was implemented at daily time-scale (Tomas-Burguera et al., 2016) prior to the aggregation to monthly scales following the recommendation of the World Meteorological Organization (WMO, 1989), using only weather stations with more than 12 months of data. The length of the available record varied between variables and the number of stations were different for each variable and varied over time. A substantial increase in the number of stations recording RH and W is noticeable toward the end of the study period, as previously highlighted by Vicente-Serrano et al. (2014b) and Azorin-Molina et al. (2016), respectively. Table 1 summarizes the number of weather stations available after quality control. The highest number of weather stations corresponded to temperature (the same number of weather stations was available for T_{min} and T_{max}) and the minimum to SD. No observed meteorological data was used for Portugal.

The Regional Climate Model (RCM) that we used in this study was HIRHAM version 5 (Christensen et al., 2006), which dynamically downscales the ERA-INTERIM model (Dee et al., 2011) for the CORDEX project (Giorgi et al., 2009). From this model we extracted gridded outputs for T_{max}, T_{min}, RH, W, and SD, which are the same variables in the observational dataset. The grids covered the IP at monthly temporal resolution and 0.11° spatial resolution for the period 1989–2011. Additionally, a digital elevation model obtained from the Spanish National Geographic Institute (IGN) was used to evaluate the mean elevation of each grid cell.

Table 1
Number of weather stations.

Variable	Number of weather stations	Simultaneous maximum
Temperature	3187	1871
Relative humidity	756	633
Wind speed	659	525
Sunshine duration	131	104

The study area, and the location of the main geographic features referenced in this paper, are presented in Fig. 1.

3. Methods

The meteorological variables described above were used as inputs to the Penman Monteith equation to obtain ET_o. We used the form of the Penman Monteith equation recommended by FAO (Allen et al., 1998). To construct the ET_o grid from information obtained at meteorological sites we used the method of OI, a data assimilation technique commonly used in the atmospheric and ocean sciences. The application of the OI algorithm to generate the ET_o grid can be done in two different ways:

1. calculate the ET_o using FAO-PM at each point with available observations and then optimally interpolate the resulting ET_o values to generate the grid; and
2. optimally interpolate the five individual meteorological fields needed to calculate ET_o, generate five interpolated grids, one per variable, and then calculate ET_o using the FAO-PM equation in the complete grids.

Previous work (Tomas-Burguera et al., 2017) has shown that although more computationally demanding, the latter approach is preferable, at least in the IP, and therefore we chose it in this study. Since in option 2) ET_o is not directly optimally interpolated, the uncertainty of each individual meteorological field needs to be propagated through the FAO-PM equation to calculate the final uncertainty of the ET_o estimates.

3.1. ET_o estimation

Allen et al. (1998) adapted the Penman–Monteith equation to a reference crop of height 0.12 m, a surface resistance of 70 $s\ m^{-1}$ and an albedo of 0.23:

$$ET_o = \frac{0.408 * \Delta * (R_n - G) + \gamma * \left(\frac{900}{T+273}\right) * U_2 * (e_s - e_a)}{\Delta + \gamma * (1 + 0.34 * U_2)} \quad (1)$$

where R_n is the net radiation at the crop surface (MJ m^{-2} day^{-1}), G is the soil heat flux density (MJ m^{-2} day^{-1}), T is the mean air temperature at 2 m (°C), U_2 is the wind speed at 2 m ($m\ s^{-1}$), e_s is the saturation vapor pressure (kPa), e_a is the actual vapor pressure (kPa), $e_s - e_a$ is the saturation vapor pressure deficit (kPa), Δ is the slope of the vapor pressure curve (kPa $°C^{-1}$) and γ is the psychrometric constant (kPa $°C^{-1}$). The value 0.408 is used to convert from MJ m^{-2} day^{-1} units to kg m^{-2} day^{-1} (alternatively: mm day^{-1}).

Some of the previous variables are not directly measured, but according to the procedure defined in Allen et al. (1998) they could be estimated using the meteorological data at hand. Specifically, T, R_n, G, e_s, e_a and Δ were estimated using SD, T_{max}, T_{min} and RH. The variable U_2 coincided with W.

The equation (Eq. (1)) is usually known as FAO-PM and is the equation we used to estimate ET_o at the monthly time-step. When necessary, we shall distinguish between ET_o computed using RCM data, $\mathbf{ET_o^b}$, and from OI data, $\mathbf{ET_o^a}$.

3.2. Optimal Interpolation

The OI equations can be easily derived as a variational problem with the goal of finding a vector of estimates that minimizes the total error variance of the field being estimated (Wikle and Berliner, 2007). The estimator is unbiased and linear between the observations and a first guess (a priori estimation) of the field. The general form of the OI equations takes the form:

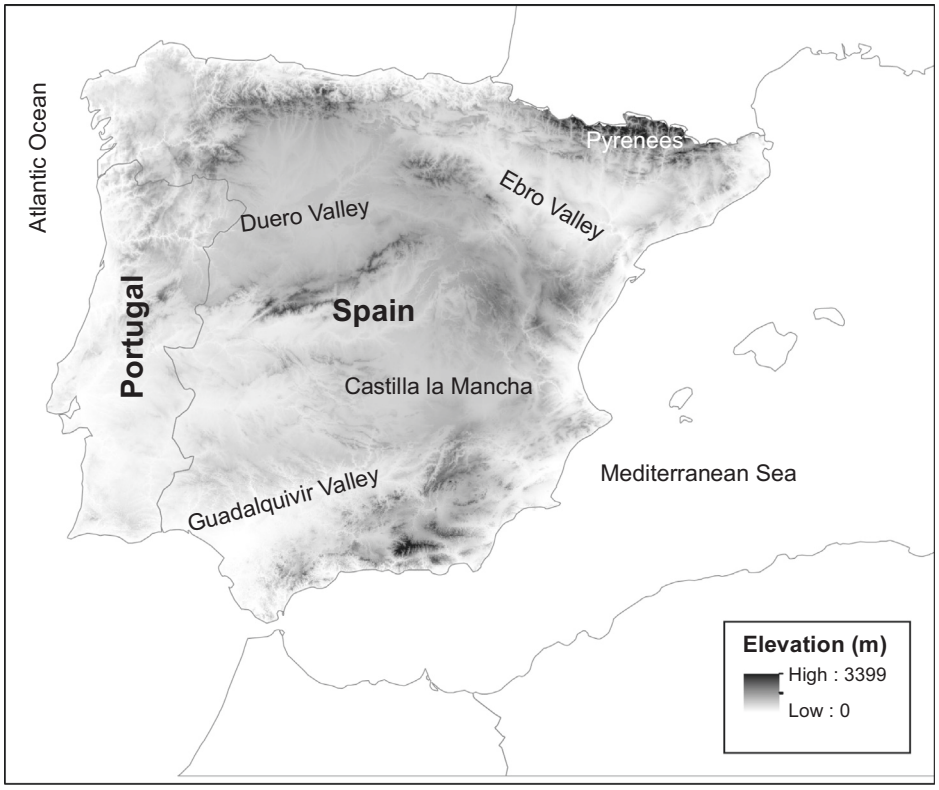

Fig. 1. Study area.

$$\begin{aligned} \mathbf{x}_v^{\mathbf{a}} &= \mathbf{x}_v^{\mathbf{b}} + \mathbf{K}_v(\mathbf{y}_v - \mathbf{H}_v\mathbf{x}_v^b) \\ \mathbf{K}_v &= (\mathbf{P}_v\mathbf{H}_v^\intercal)(\mathbf{H}_v\mathbf{P}_v\mathbf{H}_v^\intercal + \mathbf{R}_v)^{-1} \\ \mathbf{P}_v^+ &= (\mathbf{I} - \mathbf{K}_v\mathbf{H}_v)\mathbf{P}_v \end{aligned} \tag{2}$$

where the subscript v refers to each one of the meteorological variables used in the Penman Monteith equation ($T_{max}, T_{min}, RH, W, SD$) and that we are interested in optimally interpolating. Notice that we have an independent OI process for each variable; $\mathbf{x^a}$ is a vector of length m representing the final interpolated variable, i.e. the OI estimator for the variable v; $\mathbf{x^b}$ is a vector of length m representing the background or first guess of the field (in our case the RCM); $\mathbf{y}$ is a vector of length n of observations (in our case the instrumental data from the weather stations); $\mathbf{H}$ $(n \times m)$ is a sparse binary matrix to project the background data into the observation space; $\mathbf{K}$ $(m \times n)$ is the Kalman gain matrix that provides the optimal linear combination between the background and the observations; $\mathbf{P}$ $(m \times m)$ and $\mathbf{R}$ $(n \times n)$ are the error covariance matrices for the background and the observations, respectively; $\mathbf{P}^+$ $(m \times m)$ is the error covariance matrix of $\mathbf{x^a}$; and $\mathbf{I}$ $(m \times m)$ is the identity matrix. Finally, m is the grid size, which is invariant and in our case has 3930 cells, and n is the number of grid cells with observations, which varies with each variable and time step.

The results are sensitive to the values prescribed for $\mathbf{P}$ and $\mathbf{R}$, but these quantities are difficult to estimate because the amount of background (process) uncertainty associated and the observational errors are typically unknown. The parameterization of these quantities is explained later in this section.

OI assumes that both the background and the observations are unbiased with normally distributed errors:

$$\begin{aligned} \mathbf{x}_v^{\mathbf{b}} &= \mathbf{x}_v^{\mathbf{t}} + \mathbf{g}_v, \quad \mathbf{g}_v \sim \mathcal{N}(\mathbf{0}, \mathbf{P}_v) \\ \mathbf{y}_v &= \mathbf{y}_v^{\mathbf{t}} + \mathbf{e}_v, \quad \mathbf{e}_v \sim \mathcal{N}(\mathbf{0}, \mathbf{R}_v) \end{aligned} \tag{3}$$

where $\mathbf{x^t}$ is the (unknown) true value of the meteorological field, $\mathbf{y^t}$ is the (unknown) true value at grid cells with observations, and $\mathbf{g}$ and $\mathbf{e}$ are random errors normally distributed with mean 0 and covariance matrices $\mathbf{P}$ and $\mathbf{R}$, respectively. $\mathbf{P}$ and $\mathbf{R}$ are assumed to be independent from each other, a condition that is critical for the correct performance of the OI.

In this study, the background estimates of the meteorological fields ($\mathbf{x}_v^{\mathbf{b}}$ and $\mathbf{P}_v$) were obtained from the RCM. We assume that the climatologic variables of each month are random variables with stationary variance, and that each month in the record is a sample. Following this assumption, and in the absence of better information, the inter-annual variance of a meteorological variable is the most natural approximation of the uncertainty about the estimation of such variable in a given specific month and year. In other words, variables with more variance have higher uncertainty. This is further discussed in Section 4.5.

The matrix $\mathbf{P}_{\mathbf{j}_v}$ for each of the 12 months j in the record of N years can then be calculated as:

$$\mathbf{P}_{\mathbf{j}_v} = \frac{1}{N-1}\left(\mathbf{x}_{\mathbf{j}}^{\mathbf{b}}{}_v - \mathbf{1}\overline{\mathbf{x}_{\mathbf{j}}^{\mathbf{b}}}_v^\intercal\right)^\intercal\left(\mathbf{x}_{\mathbf{j}}^{\mathbf{b}}{}_v - \mathbf{1}\overline{\mathbf{x}_{\mathbf{j}}^{\mathbf{b}}}_v^\intercal\right), \quad \textbf{for } \mathbf{j} = \{1, \ldots, 12\} \tag{4}$$

where $\mathbf{x}_{\mathbf{j}}^{\mathbf{b}}{}_v$ is a matrix where each column is a cell in the grid and each row is a simulated month j in the record, $\mathbf{1}$ is a column vector of ones of size N, and $\overline{\mathbf{x}_{\mathbf{j}}^{\mathbf{b}}}_v$ is a column vector with the monthly means of each cell obtained by averaging the columns of $\mathbf{x}_{\mathbf{j}}^{\mathbf{b}}{}_v$.

For simplicity, the use of the subscript v to refer to the different meteorological variables is suppressed from now on. When necessary, explicit references to the variables will be used.

3.2.1. Observation uncertainty, R

Unlike RCM outputs, which provide meteorological estimates that are representative at the grid-cell scale, ground observations

at a location in a cell can be considered a sample of the probability distribution of the variable within that cell. This distribution is determined by the spatial variability of the meteorological variable within the cell, which is unknown. We calculated the observed estimates at each grid cell where at least one weather observation exists, and interpreted **R** as representing the uncertainty associated with the point-to-grid conversion (representational uncertainty). In other words, **R** is the uncertainty that the actual measured location is representative of the average conditions of the entire cell. Representational errors are assumed to be independent, i.e. **R** is a diagonal matrix and therefore error covariances between stations are zero. Note that since **R** is diagonal, the combination of observational information imposed by **K** on the optimally interpolated grid (Eq. (2)) is mostly controlled by the covariances of **P** (i.e. interpolation relies on the spatial covariance of the climatologic process as described by the physics of the model). Without a direct way to calculate the representational error we chose **R** to be inversely proportional to the number of stations in the monitored cell:

$$\mathbf{R} = \mathbf{I}\beta/n_{obs} \tag{5}$$

where **I** is the identify matrix of order n, β is a fixed scaling parameter that controls the magnitude of **R** and that will be used to test the impact of representational errors on the results, and n_{obs} is the number of observatories used in the estimation of **y**. The higher the number of stations in a cell, the lower the representational uncertainty.

Guided by our experience, we initially fixed β at 4.5 for T_{max} and T_{min}, 9 for *RH* and *W* and 0.9 for *SD*. To investigate the impact of scaling **R** on the results, we performed a sensitivity analysis on the choice of β as described in Section 3.4.

3.3. Uncertainty estimation

To estimate the uncertainty of $\mathbf{ET_o^a}$ we propagated the uncertainty of each one of the meteorological variables through the FAO-PM equation using a first-order method. For this we linearized the FAO-PM equation to obtain its Jacobian matrix $\mathbf{J}_{ET_o}$ and used it to propagate the covariance of the meteorological variables. For a specific location (grid-cell) k, we have:

$$(\boldsymbol{\sigma}^{\mathbf{a}}_{ET_o})^2_k = (\mathbf{J}_{ET_o})_k \mathbf{Q}_k (\mathbf{J}_{ET_o})^{\mathsf{T}}_k \tag{6}$$

where $\mathbf{Q}_k$ is the covariance matrix of the variables at location k. The Jacobian was analytically calculated with the following form:

$$(\mathbf{J}_{ET_o}) = \left[\frac{\partial ET_o}{\partial T_{max}} \quad \frac{\partial ET_o}{\partial T_{min}} \quad \frac{\partial ET_o}{\partial HR} \quad \frac{\partial ET_o}{\partial W} \quad \frac{\partial ET_o}{\partial SD} \right]$$

Assuming independence of errors between the meteorological variables, and using only the diagonal values (variances) of $\mathbf{P}^+$, i.e. $\sigma^2 \equiv diag(\mathbf{P}^+)$, the total error covariance matrix at location k is diagonal:

$$\mathbf{Q}_k = \begin{bmatrix} (\boldsymbol{\sigma}^2_{T_{max}})_k & 0 & 0 & 0 & 0 \\ 0 & (\boldsymbol{\sigma}^2_{T_{min}})_k & 0 & 0 & 0 \\ 0 & 0 & (\boldsymbol{\sigma}^2_{HR})_k & 0 & 0 \\ 0 & 0 & 0 & (\boldsymbol{\sigma}^2_{W})_k & 0 \\ 0 & 0 & 0 & 0 & (\boldsymbol{\sigma}^2_{SD})_k \end{bmatrix}$$

where the subscript k denotes we are using the scalar k element of $\boldsymbol{\sigma}^2_v$. The assumption of independence and the diagonal nature of **Q** permits to avoid operating with the full matrix **Q** and simplifies the propagation of errors. Under these assumptions, the uncertainty of $\mathbf{ET_o^a}$ can be calculated independently at each location k as:

$$(\boldsymbol{\sigma}^{\mathbf{a}}_{ET_o})^2_k = \left(\frac{\partial ET_o}{\partial T_{max}}\right)^2_k * (\boldsymbol{\sigma}^2_{T_{max}})_k + \left(\frac{\partial ET_o}{\partial T_{min}}\right)^2_k * (\boldsymbol{\sigma}^2_{T_{min}})_k + \left(\frac{\partial ET_o}{\partial HR}\right)^2_k * (\boldsymbol{\sigma}^2_{HR})_k + \left(\frac{\partial ET_o}{\partial W}\right)^2_k * (\boldsymbol{\sigma}^2_{W})_k + \left(\frac{\partial ET_o}{\partial SD}\right)^2_k * (\boldsymbol{\sigma}^2_{SD})_k \tag{7}$$

3.4. Sensitivity analysis

To assess the impact that the choice of **R** has on the results, we conducted multiple OI analyses using a range of values of β to vary de magnitude of **R**. For each interpolated meteorological variable, we tested four different values of this scaling parameter that evenly partitioned the range of **R** from an end member that represents high confidence in the observations (<**R**> $\leqslant$<**P**>) to a value that represents low confidence (<**R**> $\geqslant$ <**P**>). Table 2 shows the spatial mean values of **P** (<**P**>), which were used as a reference to design the values to scale **R**. Lowest and higher values of (<**P**>) are selected from the 12 unique (<**P**>) monthly values. β values are chosen to cover the range between a value lower than the lowest (<**P**>) value, and a value higher than the highest (<**P**>) value.

3.5. Spatial correlation with Portugal

The impact of not using weather observations over Portugal was evaluated by analyzing the spatial structure of **P**, and specifically how cells with observations in Spain covary and inform climatic estimates over Portugal. Since **R** is diagonal, the spatial structure imposed by the optimal interpolation scheme is to a large extent driven by **P**. To facilitate the spatial analysis, we first transformed our covariance matrices into correlation matrices. Then, we analyzed the number of grid points in Portugal that correlate with observed grid-points in Spain with a coefficient higher than 0.75. When grid cells in Portugal correlate highly with cells containing observations, then these observation can inform the corrections in Portugal even though they are located in Spain. During periods where correlations are lower, the quality of the estimates over Portugal decrease.

4. Results

4.1. Observational dataset

The number of instrumental observations used in the gridding process varied with time as individual stations in the network were added or decommissioned. Fig. 2 presents a time series with the number of grid cells in the domain containing one or more observations for each of the meteorological variables used in the calculation of ET_o. Temperature (T_{max} and T_{min}) had the densest spatial coverage. The number of grid cells for which temperature data were available increased from about 1200 in the late 1980s to over 1300 in 1995. From the mid-1990s, the number of stations declined steadily, and the number grid cells with temperature data was 1100–1150 toward the end of the study period. Stations that registered *RH* and *W* where less common at the start of analysis period. In the late 1980s, only about 100 grid cells contained information on these variables. The number of stations measuring *RH* and *W* increased steadily until the mid-2000s, when the installation of automatic weather stations (AWS) resulted in a sharp increase in the number of grid cells containing information. On the other hand, the number of stations measuring *SD* declined over time from about 90 stations in the late 1980s to less than 70 at the end of the study period. This decline was partly due to the obsolescence of the heliographs used to perform the measurements, which are being replaced by modern radiometers. The reason we did not

Table 2
Spatial mean values of **P** (<**P**>) and interval of tested β values.

Variable	<**P**> values		β tested values			
	Lowest value	Highest value	1st	2nd	3rd	4th
T_{max}	1.1	4	0.9	3.6	6.3	9
T_{min}	1.3	3	0.9	3.6	6.3	9
RH	28	48	9	36	63	90
W	0.06	0.37	0.009	0.09	0.9	9
SD	0.03	0.74	0.009	0.09	0.9	9

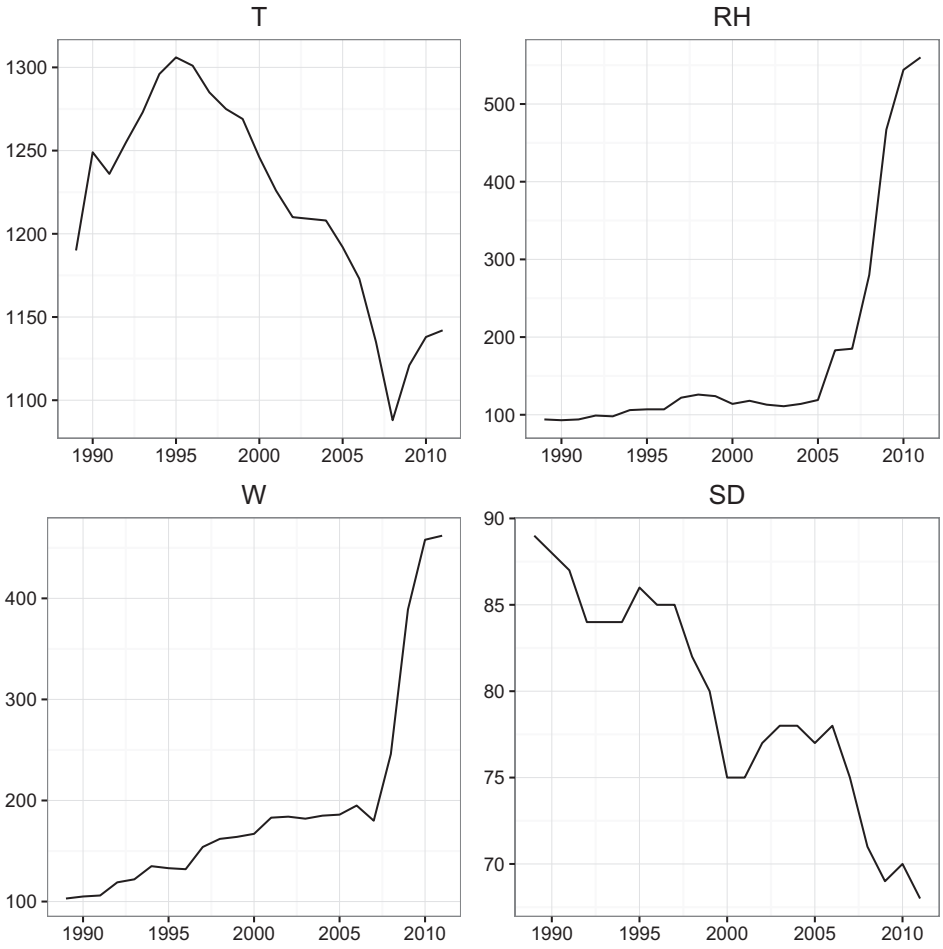

Fig. 2. Time series of the number of grid cells containing at least one weather station (*n*) for temperature, *T*; relative humidity, *RH*; wind speed, *W*; and sunshine duration, *SD*.

include information from radiometers is that only heliographs provide a homogeneous dataset that covers the entire study period.

4.2. Optimally interpolated climatic variables and ET_o estimates

The proposed method produces gridded fields of mean ($\mathbf{x^a}$) and variance $(\boldsymbol{\sigma}^a)^2$ estimates for each climate variable and for ET_o ($\mathbf{ET_o^a}$ and $(\boldsymbol{\sigma}^{\mathbf{a}}_{ET_o})^2$). To illustrate the outcome of the process and provide a sense of the typical spatial distribution of the estimates and their associated uncertainty, results are presented for one sample month, July 1994 (Fig. 3). Overall, the estimates for all meteorological variables and for ET_o show spatial structure devoid of the interpolation artefacts often produced by other interpolation methods. The expected spatial climatologic patterns of the variables over the IP are captured, including very localized windward-leeward effects produced by the rugged physiography of mountain regions. In this sample month, the highest temperatures are located in the southern region of the peninsula and in the Ebro Valley in the northeast. High $\mathbf{x}^{\mathbf{a}}_{RH}$ values are concentrated in regions close to the coast and along corridors that extend the oceanic influence further inland. Wind speed, $\mathbf{x}^{\mathbf{a}}_{W}$, is highest in the Castilla la Mancha region (eastern Spain), and in the Ebro Valley in northeastern Spain, where high wind speeds are facilitated by the unobstructed high plateau of Castilla, and by accelerations of northern winds in the Ebro Valley due to the interaction between the orographic dipole of the Pyrenees mountain range with the morphology of the Ebro catchment (Riosalido et al., 1986).

Finally, sunny summers and the compact shape of the IP produce similar mean $\mathbf{x}^{\mathbf{a}}_{SD}$ estimates in July, with the exception of the coastal northern region where mean $\mathbf{x}^{\mathbf{a}}_{SD}$ values are significantly lower due to persistent cloud cover. The climatology described by these variables produces $\mathbf{ET_o^a}$ estimates that are higher in the southern region and in the Ebro valley, and lower in the north

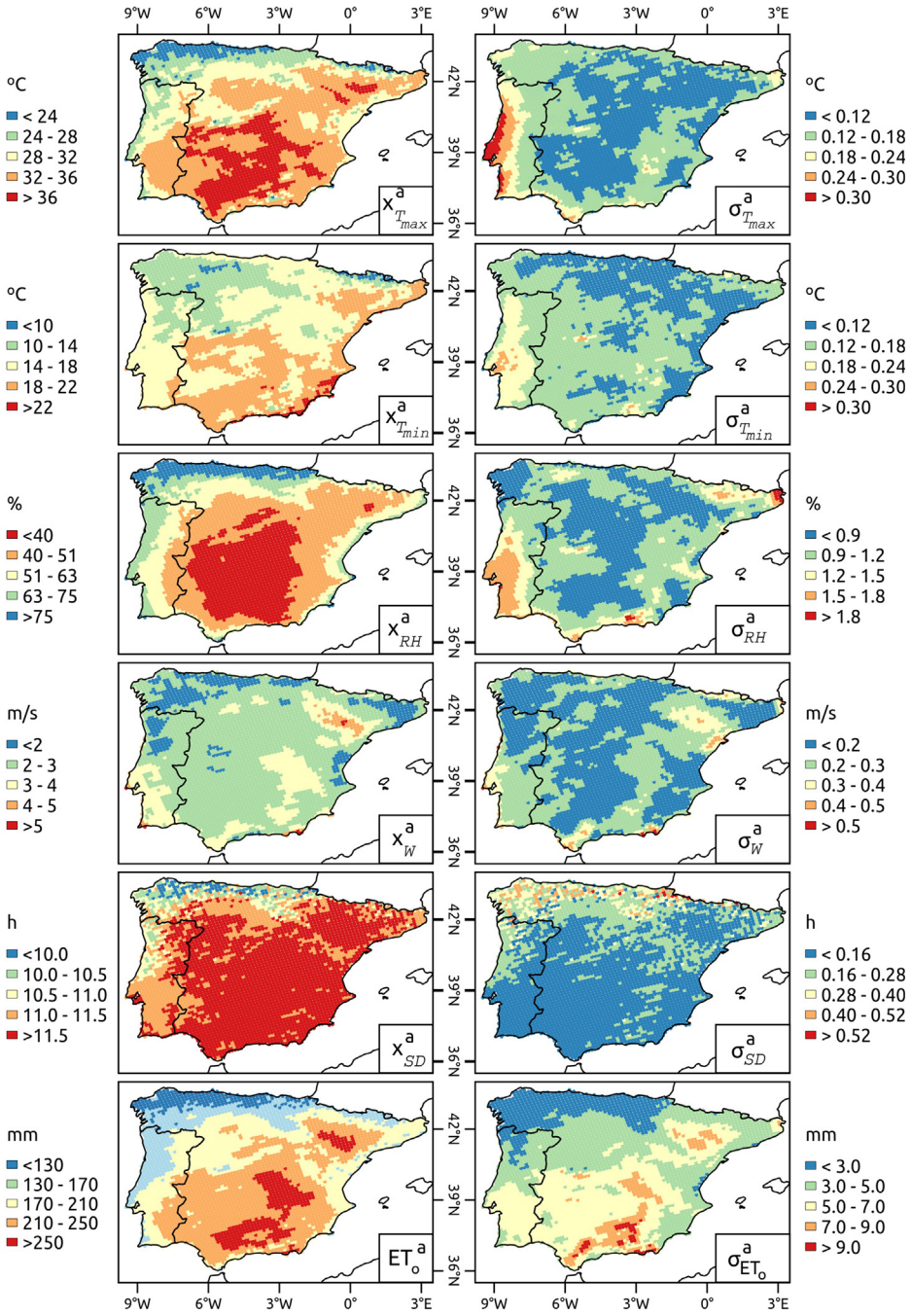

Fig. 3. OI estimated mean values ($\mathbf{x}^{\mathbf{a}}_v$) and standard deviation ($\boldsymbol{\sigma}^{\mathbf{a}}_v$) of maximum temperature (T_{max}); minimum temperature (T_{min}); relative humidity (RH); wind speed (W); sunshine duration (SD) and reference evapotranspiration ($\mathbf{ET^a_o}$ and $\boldsymbol{\sigma}^{\mathbf{a}}_{ET_o}$), for the month of July 1994.

and northwest region of the peninsula. The uncertainty of these estimates, represented as the standard deviation $\boldsymbol{\sigma}^{\mathbf{a}}$, are in general low due to the relatively high number of instrumental observations available and the high spatial correlation of the variables. This is especially true for $\boldsymbol{\sigma}^{\mathbf{a}}_{T_{max}}$ and $\boldsymbol{\sigma}^{\mathbf{a}}_{T_{min}}$, for which typical values were lower than 0.3 °C. $\boldsymbol{\sigma}^{\mathbf{a}}_{RH}$ presents higher values in the southwest and northeast. This study did not use observations in Portugal, which is the reason why these variables show higher uncertainty in the west and southwestern regions of the IP. Relatively high values of $\boldsymbol{\sigma}^{\mathbf{a}}_W$ are present only in the regions with highest wind speeds. The northwestern and northern coastal regions, where cloud cover is most variable, result in the highest values for $\boldsymbol{\sigma}^{\mathbf{a}}_{SD}$. Because the FAO-PM equation is non-linear and concave upward, uncertainties are amplified in regions of high ET_o, where the function tends to have steeper derivatives.

To illustrate the typical time series generated by our method for each meteorological variable and for $\mathbf{ET^a_o}$. Fig. 4 presents results for one sample location in central Spain. The most prominent feature of estimates for $\mathbf{x}^{\mathbf{a}}_{T_{max}}$, $\mathbf{x}^{\mathbf{a}}_{T_{min}}$, $\mathbf{x}^{\mathbf{a}}_{SD}$, and $\mathbf{ET^a_o}$ is the expected and marked seasonality with summer peaks and winter lows. An inverse seasonality affects $\mathbf{x}^{\mathbf{a}}_{RH}$, with summer lows and winter peaks, whereas $\mathbf{x}^{\mathbf{a}}_W$ does not show seasonality. The most interesting information in this figure is the standard deviation of the estimates $\boldsymbol{\sigma}^{\mathbf{a}}$, which shows that uncertainty has a clear dependency on time (seasonality) for all variables. In addition, $\boldsymbol{\sigma}^{\mathbf{a}}_{RH}$, and to a lesser degree $\boldsymbol{\sigma}^{\mathbf{a}}_W$, exhibit a marked decrease in the standard deviation of the

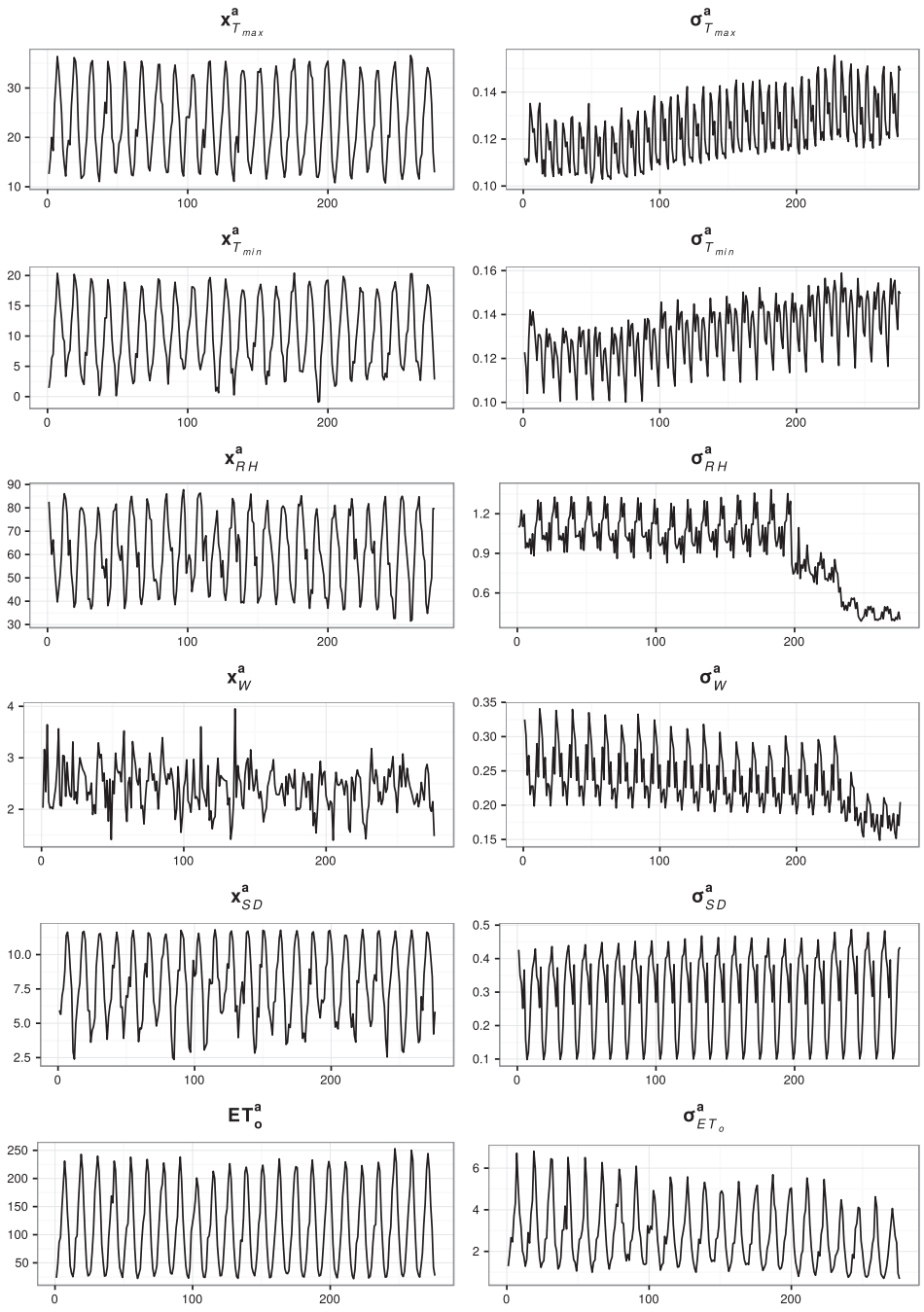

Fig. 4. Time series of OI estimated mean values ($\mathbf{x}^{\mathbf{a}}_{v}$) and standard deviation ($\boldsymbol{\sigma}^{\mathbf{a}}_{v}$) of maximum temperature (T_{max}); minimum temperature (T_{min}); relative humidity (RH); wind speed (W); sunshine duration (SD) and reference evapotranspiration ($\mathbf{ET}^{\mathbf{a}}_{\mathbf{o}}$ and $\boldsymbol{\sigma}^{\mathbf{a}}_{ET_o}$), at one random grid cell.

estimates toward the last quarter of the study period, while $\boldsymbol{\sigma}^{\mathbf{a}}_{SD}$ shows a moderate increase over time. These trends are associated with variations in the number of data points used to perform the interpolation, as we will discuss later. Seasonality and trends in the uncertainty of individual climate variables are propagated to $\boldsymbol{\sigma}^{\mathbf{a}}_{ET_o}$, which in general also shows a clear seasonality and a decline toward the last quarter of the period.

4.3. Comparison between OI and the RCM

The analysis of differences $\boldsymbol{\delta} = \mathbf{x}^{\mathbf{a}} - \mathbf{x}^{\mathbf{b}}$ between the OI and the background RCM is of interest for detecting possible biases in the RCM, and also to evaluate the adequacy of the observational network. Fig. 5 shows $\overline{\mathbf{x}^{\mathbf{a}}}$ (the mean of $\mathbf{x}^{\mathbf{a}}$ over time) and $\overline{\mathbf{x}^{\mathbf{b}}}$ (the same for $\mathbf{x}^{\mathbf{b}}$) for each climate variable and for ET_o ($\overline{\mathbf{ET}^{\mathbf{a}}_{\mathbf{o}}}$ and $\overline{\mathbf{ET}^{\mathbf{b}}_{\mathbf{o}}}$), as well as their differences $\overline{\boldsymbol{\delta}}$. In general, the RCM tended to underestimate T_{max} ($\overline{\boldsymbol{\delta}_{T_{max}}} > 0$) and to overestimate T_{min} ($\overline{\boldsymbol{\delta}_{T_{min}}} < 0$), indicating that the RCM describes a shallower annual temperature range than the observations. We should keep in mind, though, that the RCM output represents mean cell estimates, which are expected to have a lower variability than the very local (point) information represented by the observations. For RH, the OI estimates present higher values ($\overline{\boldsymbol{\delta}_{RH}} > 0$) in the southern region of the IP, and lower values in the northern part ($\overline{\boldsymbol{\delta}_{RH}} < 0$). For W the biggest differences appeared in the north-east region, specially along the Ebro Valley.

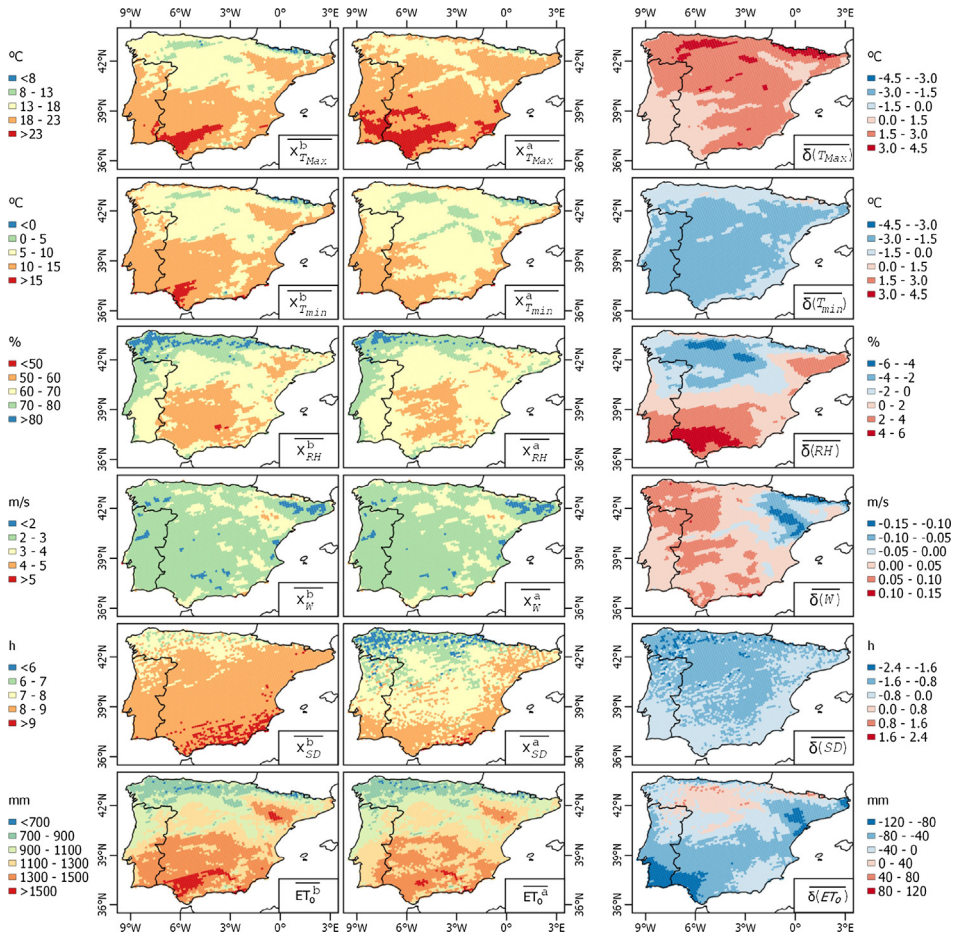

Fig. 5. Mean annual values of OI estimated and background RCM ($\overline{\mathbf{x}_p^a}$ and $\overline{\mathbf{x}_p^b}$, respectively) of maximum temperature (T_{max}); minimum temperature (T_{min}); relative humidity (RH); wind speed (W); sunshine duration, (SD); and reference crop evapotranspiration ($\overline{\mathbf{ET_o^a}}$ and $\overline{\mathbf{ET_o^b}}$), and the differences between them ($\overline{\boldsymbol{\delta}}$).

Lower values of SD ($\overline{\delta_{SD}} < 0$) appeared in the northern region, which could be related to the presence of low level clouds not easily resolved by RCMs.

The effect of these differences is only modestly apparent in the mean ET_o of the study period. The method corrects an $\overline{\mathbf{ET_o^b}}$ overestimation ($\overline{\delta_{ET_o}} < 0$) in the southern region of the IP and in the Ebro Valley, and corrects an underestimation ($\overline{\delta_{ET_o}} > 0$) in the northern region and mountainous areas. $\overline{\mathbf{ET_o^a}}$ presents higher values in the northern region and lower values in the southern region. In general, it appears that the spatial pattern of $\overline{\delta_{ET_o}}$ is very similar to the pattern of $\overline{\delta_{RH}}$, suggesting that this variable is a major player in determining the spatial patterns of the atmospheric water demand in the region.

The domain-wide seasonal amount of correction is depicted in Fig. 6, which presents monthly $<\overline{\mathbf{ET_o^a}}>$ and $<\overline{\mathbf{ET_o^b}}>$. In general, the mean values are similar except during spring and autumn, where $\overline{\mathbf{ET_o^b}}$ seems to overestimate regional mean values. The figure also presents the spatial interquartile range. Here also, the largest differences between the two datasets occur during spring and autumn. During these months, the spatial variability of $\overline{\mathbf{ET_o^a}}$ is smaller than that represented by $\overline{\mathbf{ET_o^b}}$.

4.4. Impact of the number of available observations

As described in Section 4.1, the number of stations providing meteorological information varies over time, being most prominent the increase in the number of stations measuring RH and W. In standard interpolation methods, the granularity of the resulting fields is highly dependent on the number and spatial distribution of the observational data used for interpolation. This is a problem because it also generates trends in the dispersion statistics (variance, kurtosis) of the spatial fields. We evaluate the extent to which OI reduces this problem by analyzing the impact of the number of observations on the amount of correction that our methods apply to the RCM estimates, and on the spatial variance of the corrected fields.

Fig. 7 shows time series of the spatial mean of the correction applied to the RCM, $<\boldsymbol{\delta}_{ET_o}>$. The differences are grouped by months to remove the seasonal cycle. While a strong variability in the mean correction is detected in some months, no trends are apparent in the time series, not even in the last quarter of the period when a sharp increase in the number of RH and W weather stations took place. We also analyzed if the varying number of stations used in the OI process generated temporal trends in the spatial variability of the $\mathbf{ET_o^a}$ field. Fig. 8 shows time series of the standard deviation of the field, also grouped by months. An inspection of the figure shows that only seasonal patterns exist, and that no apparent trends can be identified that reveal an increase or decrease in the variability of the field as the number of observations used for interpolation changed over the years.

While the mean estimates did not seem sensitive to the number of stations used in the OI process, the same was not true for their uncertainty. Fig. 9 show time series of the spatial mean of the uncertainty of meteorological variables $<\boldsymbol{\sigma}^{\mathbf{a}}>$ and of ET_o, $<\boldsymbol{\sigma}^{\mathbf{a}}_{ET_o}>$.

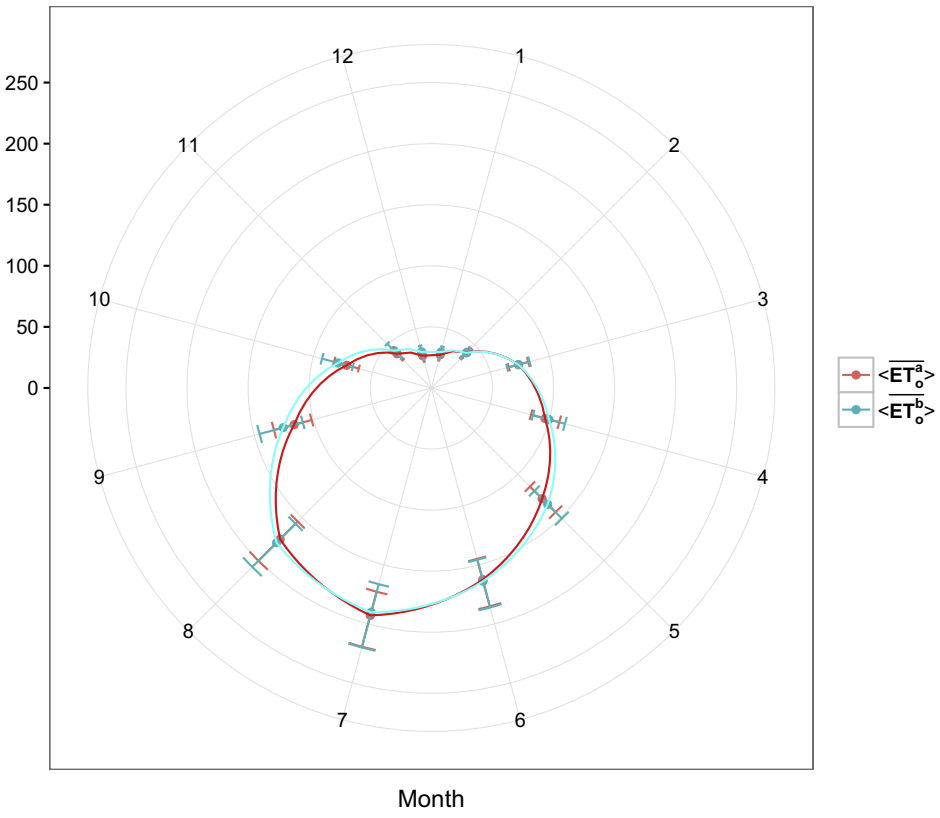

Fig. 6. Monthly spatial mean values of OI estimated and background RCM reference crop evapotranspiration (<$\overline{\mathbf{ET_o^a}}$> and <$\overline{\mathbf{ET_o^b}}$>, respectively). The error bars indicate the spatial interquartile range.

In the figure we see that <$\boldsymbol{\sigma}^{\mathbf{a}}_{ET_o}$> follows the same seasonality of the mean values, showing higher uncertainty during the summer months and lower in winter, but the overall uncertainty decreased over the years as the available information used to condition the RCM field increased. The Man-Kendall trend test (Man, 1945; Kendall, 1975), with a significance level $\alpha = 0.05$, determined that the negative trend in the mean spatial uncertainty <$(\boldsymbol{\sigma}^{\mathbf{a}}_{ET_o})^2$> is significant for all the months except for June (Table 1 Anex). The decrease in <$\boldsymbol{\sigma}^{\mathbf{a}}_{ET_o}$> seems to be most related to the sharp decrease in <$\boldsymbol{\sigma}^{\mathbf{a}}_{RH}$> and <$\boldsymbol{\sigma}^{\mathbf{a}}_{W}$> as the number of observations for these two variables increase. This occurs despite the fact that the <$\boldsymbol{\sigma}^{\mathbf{a}}_{T_{max}}$>, <$\boldsymbol{\sigma}^{\mathbf{a}}_{T_{min}}$> and <$\boldsymbol{\sigma}^{\mathbf{a}}_{SD}$> increase as the number of available observations declined. The highest uncertainty in the temperature estimates occurred during the warmest months of the year, with a secondary peak in winter for <$\boldsymbol{\sigma}^{\mathbf{a}}_{T_{min}}$>. On the other hand, <$\boldsymbol{\sigma}^{\mathbf{a}}_{W}$> and <$\boldsymbol{\sigma}^{\mathbf{a}}_{SD}$> showed higher values in winter and lower values in summer. <$\boldsymbol{\sigma}^{\mathbf{a}}_{RH}$> showed no seasonality, having similar values throughout the year.

4.5. Impact of R

Figs. 10 and 11 present, respectively, the time series of the spatial mean of estimates for each meteorological variable, <$\mathbf{x}^{\mathbf{a}}$>, and of the spatial mean of their associated posterior standard deviation, <$\boldsymbol{\sigma}^{\mathbf{a}}$>, for each of the four tested **R** matrices.

In general we found that the results estimates remained robust for the range of **R** matrices tested and only $\mathbf{x}^{\mathbf{a}}_{W}$ and $\mathbf{x}^{\mathbf{a}}_{SD}$ showed relevant differences. In the case of $\mathbf{x}^{\mathbf{a}}_{W}$, differences appeared only in the first years of the study when the number of available observations was similar to those of *SD*. As the number of *W* observations increased, the effect of **R** on $\mathbf{x}^{\mathbf{a}}_{W}$ faded out, and similar results were obtained for the different matrices. On the other hand, the sensitivity of $\mathbf{x}^{\mathbf{a}}_{SD}$ on **R** remained since the number of observations available of this variable continued to decline. This suggests the existence of an observation density threshold beyond which the impact of observation uncertainties on the OI estimation process is limited. The magnitude of **R** has a more severe impact on the spatial mean of the estimate uncertainty, <$\boldsymbol{\sigma}^{\mathbf{a}}$>. As expected, larger **R** values resulted in larger uncertainties, with a clear dependency on the number of available observations. This effect was most clear on <$\boldsymbol{\sigma}^{\mathbf{a}}_{RH}$> and <$\boldsymbol{\sigma}^{\mathbf{a}}_{W}$>, since these two variables experienced the sharpest increase in the number of observations during the study period. It is worth noting that the values of <$\boldsymbol{\sigma}^{\mathbf{a}}_{RH}$> at the end of the period in the worst-case scenario (largest **R**) were similar to those at the start of the period in the best-case scenario (lowest **R**), which suggests the existence of a trade-off between the quantity and the quality of the observations.

4.6. Portugal correlation analysis

Fig. 12 shows the results of the spatial correlation analysis over Portugal for all the variables in two contrasting months, January and July. The color in each cell indicates with how many of the 600 grid-cells over Portugal the cell has a correlation higher than 0.75. In January (winter), large areas of Spain show high correlation with Portugal. In all cases, and not surprisingly, western Spain is the most correlated region with Portugal. T_{max} and T_{min} are the variables exhibiting the most extensive correlation.It is interesting that *RH* and *SD* during the month of January show a region of extensive correlation with Portugal in the southern face of Pyrenees range. This is mostly explained by the orographic uplift of southern winds

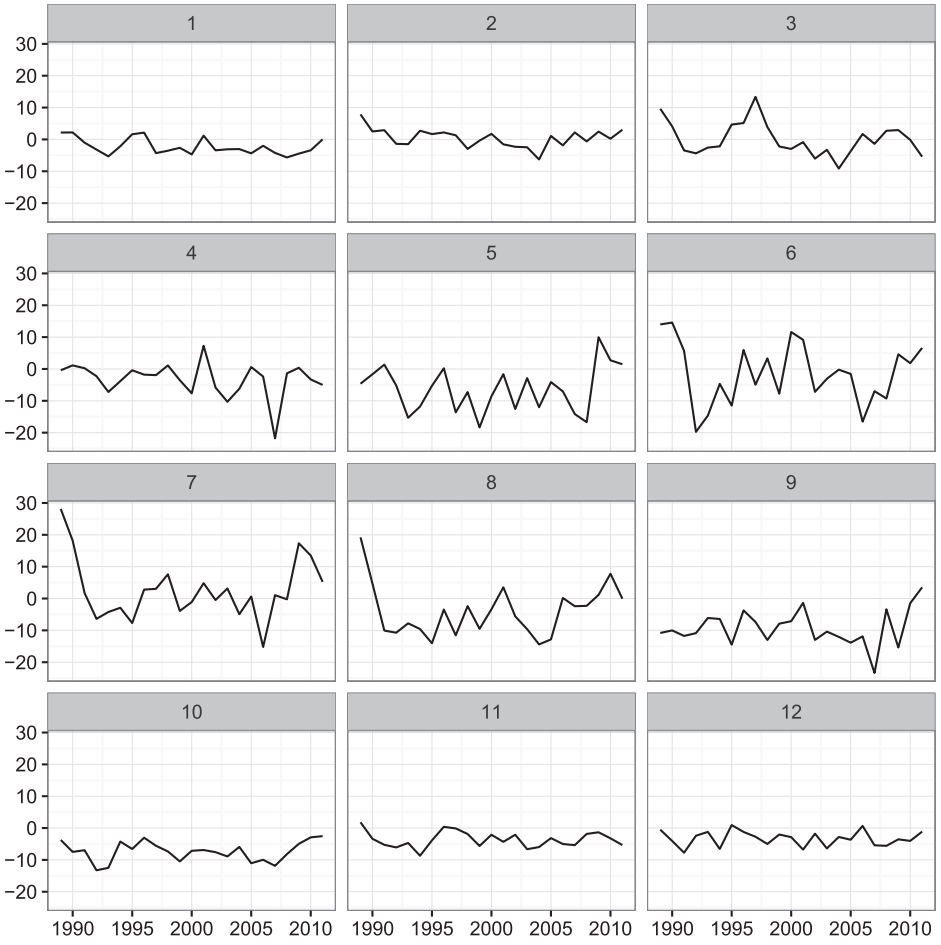

Fig. 7. Time series of the spatial mean correction applied to the RCM, $\langle \delta_{ET_o} \rangle = \langle \mathbf{ET_o^a} - \mathbf{ET_o^b} \rangle$, for each month (1 indicating January, etc).

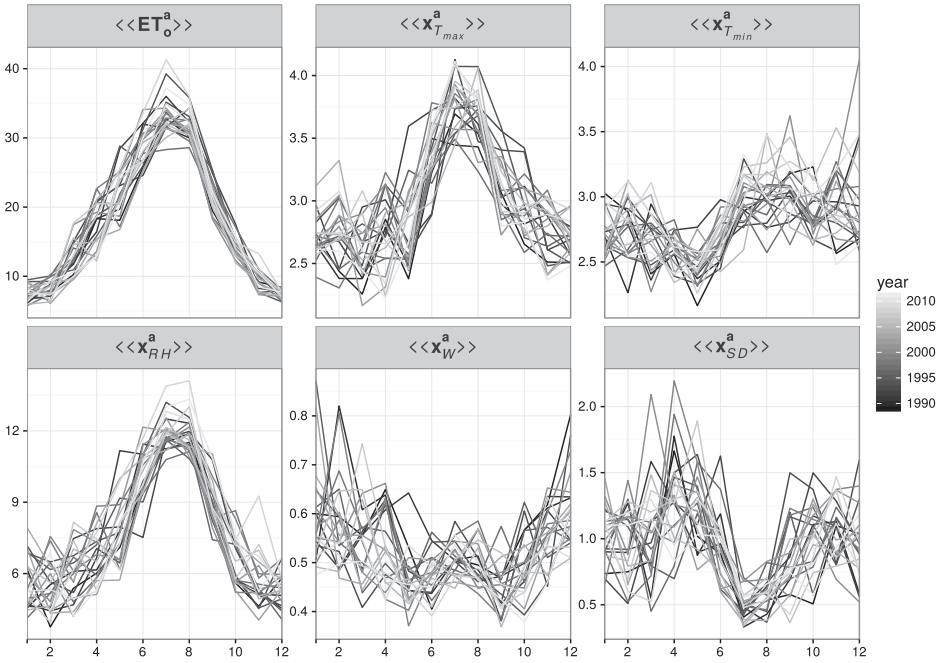

Fig. 8. Time series of the spatial standard deviation of input variables ($\ll \mathbf{x}_i^a \gg$) and ($\ll \mathbf{ET_o^a} \gg$). Different shades of gray indicate years, and the months are in the x-axis (1 indicating January, etc).

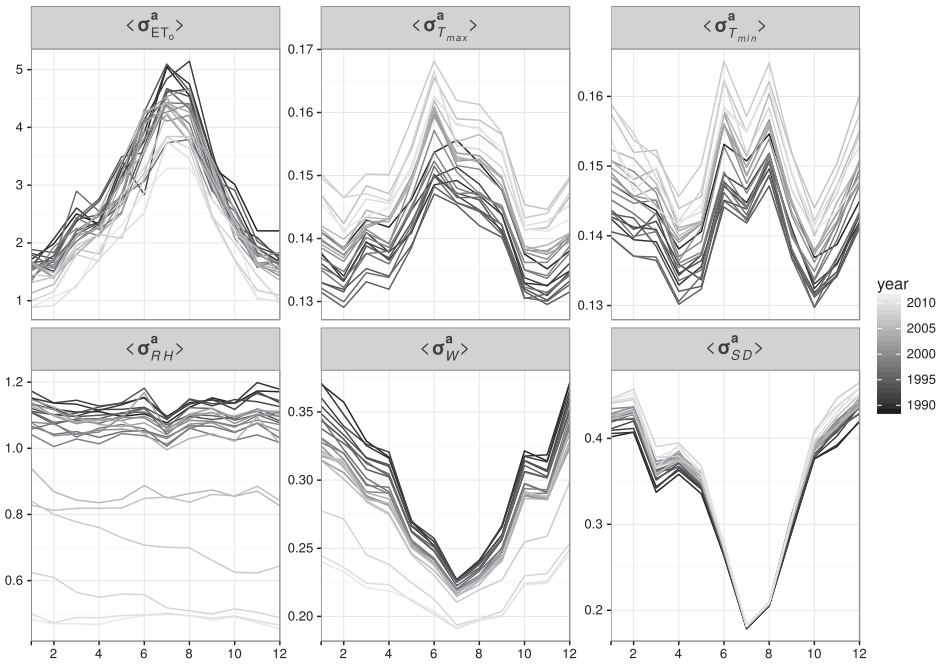

Fig. 9. Time series of the spatial mean of the uncertainty of climate variables, $<\boldsymbol{\sigma}^{\mathbf{a}}>$, and ET_o, $<\boldsymbol{\sigma}^{\mathbf{a}}_{ET_o}>$. Different shades of gray indicate years, and the months are in the x-axis (1 indicating January, etc).

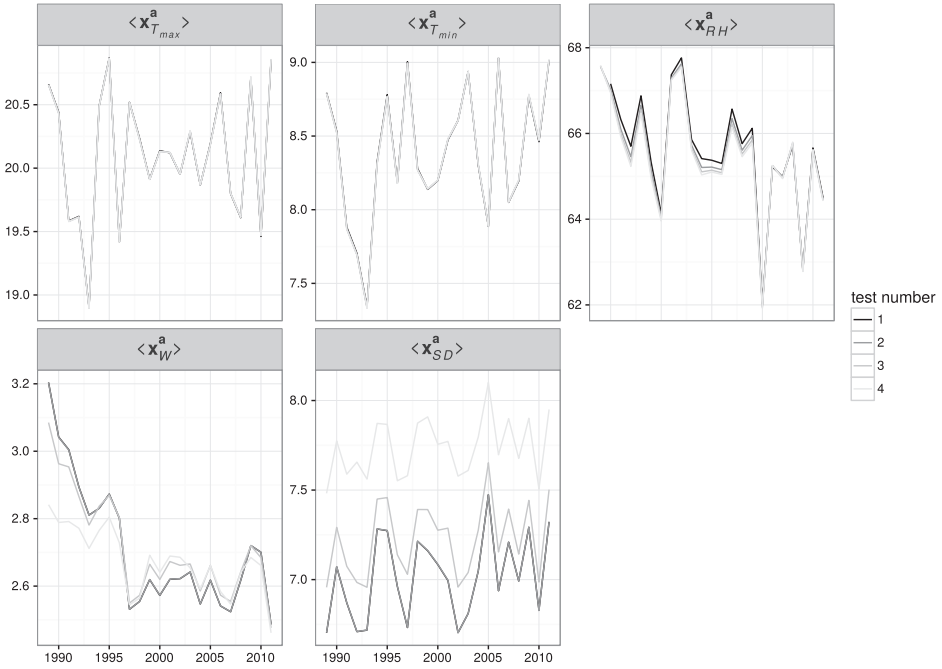

Fig. 10. Time series of spatial mean values of each climatic variable ($<\mathbf{x}^{\mathbf{a}}_{v}>$), as a function of different values of β. The exact values of β for each variable and test number are given in Table 2.

in this region, which occur simultaneously with cyclonic conditions affecting the western part of IP. on the other hand, correlated areas tend to decrease in July (summer) for all variables and the correlations are more spatially restricted to the western area of Spain. The decrease in the extension of highly correlated areas is specially acute for *SD*, which is explained by the fact that cloudiness during summer months is often related to local or subregional conditions (i.e. mainly convection and sea fog interacting with coastal areas).

From these results, we consider that obtaining good climatological and ET_o estimates over Portugal using observations located in Spain is possible, but these estimates are expected to be of better quality during winter, when synoptic conditions over IP is highly correlated. Unfortunately, ET_o estimates are most relevant during the summer months, when AED is high (Fig. 6). During summer local conditions become more important and correlations between Portugal and the rest of the IP become more fragmented.

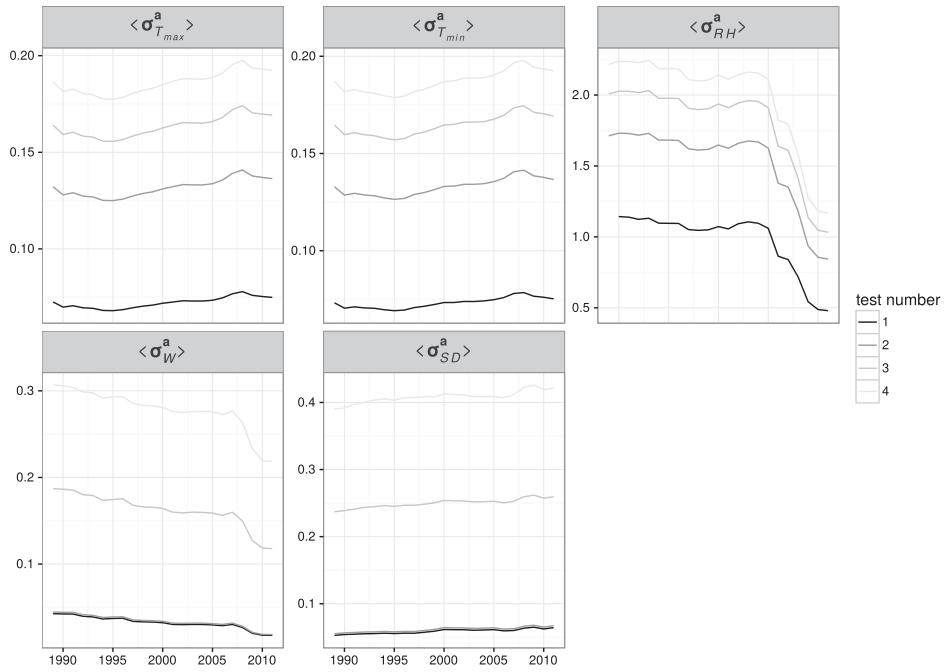

Fig. 11. Time series of spatial mean values of uncertainty of each climatic variable ($<\sigma^a_v>$), as a function of different values of β. The exact values of β for each variable and test number are given in Table 2.

5. Discussion

5.1. Meteorological estimates

The mean climatic fields presented in Fig. 5 describe the climatology of the IP. The northern and northwestern regions are the wettest and coolest, with the lowest values of ET_o, SD, and T_{max} and T_{min}, and higher values of RH. The highest T_{max} and T_{min} are mostly concentrated in the southern half, with the Guadalquivir River valley standing out, with the exception of the Ebro River valley in the northeast, which forms a depression with a characteristic semi-arid local climate.

Obtained values of ET_o are in concordance with previous studies in the Iberian Peninsula, taking into account that other studies were developed using only a subset of weather stations (Vicente-Serrano et al., 2014c used 46 weather stations in the Spanish part of the IP) or only analyzed a subregion in the IP (such as Vanderlinden et al., 2008 and Espadafor et al., 2011, who analyzed only Andalusia). The same spatial distribution of ET_o was detected by some of those previous works. The higher values appear in the southern region and the lower values in the northern region of the IP. The Ebro Valley, a region located in the north, is an exception to this latitudinal pattern, showing high values of ET_o. The absolute values detected in our study are quite similar to the values of previous studies, with maximum values higher than 1400 mm in the Guadalquivir Valley, and values lower than 1000 mm in the northern region. Our results show somewhat higher values in the southern region, up to 1600 mm at some locations in the Guadalquivir Valley. Some reasons for these higher estimates are: i) We used all the weather stations available; ii) 1961–2011 period show a clear positive trend in ET_o, as detected by Espadafor et al. (2011) and Vicente-Serrano et al., 2014a, and our study period (1989–2011) is the last part of that period. Because of that we possibly detected higher mean values than previous studies in some regions. On the other hand, minimum values below 700 mm in mountainous regions would be in agreement with the detection of low values in Sierra Nevada done by Vanderlinden et al. (2008).

The seasonality of ET_o (Fig. 6) follows the well-known seasonal cycles of T_{max}, T_{min} and SD, with highest ET_o in the summer and lowest during the winter months (Espadafor et al., 2011; Vicente-Serrano et al., 2014c; Martins et al., 2017). The higher spatial variability of summer months was also detected in those previous studies.

The correction that meteorological observations impose on the background RCM can be analyzed by the differences between the meteorological fields estimated by the OI and those from the RCM. These differences often present systematic patterns that can be attributed to biases in the RCM, as found by Kotlarski et al. (2014); but they could also be attributed to the impact of correcting the field with observations that have a footprint smaller than the grid cells. The spatial and temporal variability expected from ground observations is larger because their footprint is representative of a region much smaller than that of the grid cell. For instance, optimally interpolated annual mean values of T_{max} are higher than those of the RCM, while mean values of T_{min} are lower, indicating that the RCM tends to dampen thermal oscillations in most of the spatial domain. This correction is spatially consistent, except perhaps in high elevation regions. The only variable that shows very contrasting spatial corrections of different sign is RH, since OI tend to increase the lower values of RH in the northern half of the IP and decrease the highest values in the south. This spatial correction pattern of RH is very similar to the differences in the mean ET_o field calculated from the OI variables and from the ET_o calculated from the uncorrected RCM variables, which reinforces the conclusions by Azorin-Molina et al. (2015) that RH is a key driver of ET_o in the IP.

Regarding SD, annual mean values in the OI field are generally lower than those estimated by the RCM. Two main factors could help explain differences in SD: i) the WMO defined SD as the time interval in which the solar radiation exceeds 120 Wm^{-2} (WMO, 2003). While SD obtained from the RCM considers this, the observed SD data is more subjective for the period when the Campbell-Stokes (CS) recorder was used. Kerr and Tabony (2004) compared the perfomance of CS and automatic sensors obtaining

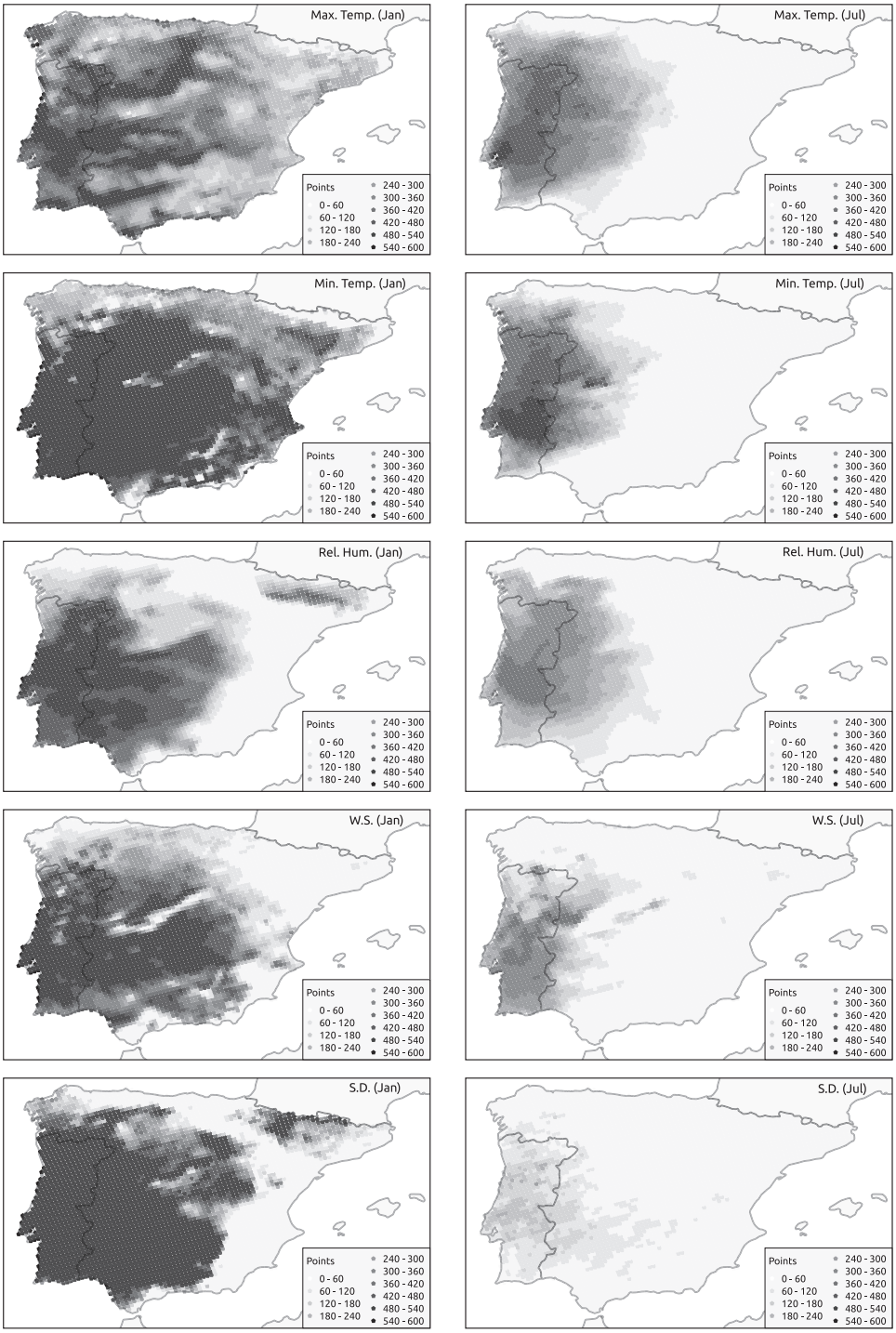

Fig. 12. Number of Portuguese grid points for which the correlation coefficient is higher than 0.75 for each grid point in Iberian Peninsula.

a good agreement, but with some differences perhaps because the solar radiation at which the CS starts to record ranges from 106 to 285 W m^{-2} (Painter, 1981); and, ii) the general over-prediction of solar radiation affecting climate models could also be affecting the RCM used in this study (Wild et al., 2013). In fact, our correction of *SD* values are in concordance with the results obtained for solar radiation by Ruiz-Arias et al. (2015).

Finally, while we expected higher spatial variability of *W* in the observational dataset than in the RCM, the annual mean values of the OI fields are lower than those of the RCM. Wind speed is a complex variable, with high local spatial variability that physical models find difficult to capture. In fact, some authors (e.g. Ishak et al., 2010) detected that dynamically downscaling a global reanalysis did not improve the quality of the *W* field with respect to the original reanalysis. Moreover, an experiment using the WRF (Skamarock and Klemp, 2008) Regional Climate Model in the north of the IP by Jiménez and Dudhia (2012) showed that wind speeds calculated at grid points were poor predictors of values observed at the closest ground observatories.

In the IP, Martins et al. (2017) tested a blended reanalysis developed by Sheffield et al. (2006), which combined data from distinct sources to obtain a global reanalysis of better quality than any of

the individual sources. Usually, the global products have a coarser spatial resolution (0.5° in this case), than regional products (0.11° for our product). While they used weather observations to validate the results they obtained, we preferred not to do that because the value of a weather observation refers to an exact point, while the values of OI refer to a grid cell. Nevertheless, as it has been previously explained, both the spatial and temporal distribution of our product are coherent with results obtained by previous studies.

5.2. Uncertainty of estimates

Our methodology makes a number of assumptions that are worth discussing before interpreting the results. We consider that the uncertainty of background (RCM) estimates **P** equals to their monthly variance. This assumption is based on the idea that monthly estimates of a variable are random variables, and that each year in the RCM record is one sample of the variable for each month. Under this assumption and in the absence of additional information, the historical variability (the sample variance) of the RCM estimates for a given month of the year is the uncertainty around the estimate of this variable. Note that we are not inferring monthly climatologic means, whose uncertainty is represented by the standard error of the mean, but values for each particular month in the record, so the sample variance (the climatological variability) and not the standard error is a more appropriate measure of their uncertainty.

We believe this choice provides a conservative (pessimistic) estimate of the background uncertainty because it does not leverage information available from previous months.

An alternative approach to parameterize **P** would be to use the variance from an ensemble of models (e.g. from the CORDEX project). We argue that this approach would underestimate the actual uncertainty of the estimates because the limited number of models included in the ensemble, and because the finite conceptualisations of the reality that they implement, sample only a limited range of the actual uncertainty (Knutti, 2010). For this, and for its simplicity, we preferred to provide the initial estimate of uncertainty from the monthly climatology of the RCM. Recently, the ERA5 (new reanalysis of the ECMWF) was made available for the period 2010–2016, and includes a measure of its uncertainty. A comparison between both approaches to parameterize **P** will be possible when the full temporal record in the ERA5 dataset becomes available (Hersbach and Dee, 2016).

A second relevant consideration is the prescription of matrix **R**, which represents the error variance of the observations. We assumed that observational or instrument errors, which are seldom documented, are negligible compared to the station representativity error, which quantifies the uncertainty associated with the local conditions measured by a given station being representative of the cell where the station is located. To approximate this uncertainty we assumed that station errors are independent from each other (i.e., that the matrix **R** is diagonal), and that the uncertainty of each station is inversely proportional to the number of data occurring inside a specific grid cell, such that the higher the number of observatories used to estimate the mean value of a grid cell the lower the observational uncertainty for that cell.

Fig. 10 shows that variables that are sampled by a large number of stations (T_{min} and T_{max}), variations in **R** affect only the uncertainty while the estimates themselves are not affected. This is because errors in **R** are assumed to be unbiased and independent, which along with the large number of available stations and the high spatial covariation imposed by **P** allows for a robust estimation of the spatial field. On the other hand, variables with a smaller number of observations such as *RH*, *W* and *SD* show that variations in **R** affect both the estimate's uncertainty and the estimates themselves. Interestingly, the case of *RH* and *W*, both of which experienced a large increase in the number of available observations over time, suggests that there is a threshold in the number of observations beyond which the estimates are mostly unaffected by observation uncertainty. This is indicative of a trade-off between the quantity and the quality of observational information, as we will discuss below.

5.3. Impact of changes in the density of the observational network

The generation of meteorological grids using standard interpolation methods, such as kriging and other methods based on distance weighting, is very sensitive to variations in the number and location of the weather stations used. Moreover, the density and distribution of ground observations necessary to resolve the spatial variability of the climatic field being reconstructed depends on the degree of spatial autocorrelation of the field. This is because the covariance of the process determines the size of the region each observation is representative of Silverman and Maneta (2016). This has non-trivial consequences for any climate analysis performed using these grids, because the varying number of stations used for interpolation may induce trends in the spatial variability (granularity) of the meteorological fields that can easily be misinterpreted as being genuinely caused by a climatic process.

Our analysis (Fig. 8) showed that the spatial standard deviation of the fields produced by OI was not as acutely affected by this problem as traditional interpolation methods are, as demonstrated in previous studies (Beguería et al., 2016). While the rapid increase in the number of observations affected the estimates of *RH*, *W* and *SD* (Fig. 2), the spatial variance of these fields did not show appreciable changes that could be attributed to the densification of the observational network. For *RH* and *W*, which more than doubled the available data in the last 5 years of the study period, an increase of the granularity of the field could be expected, due to more local effects being detected within the observational network. On the other hand, *SD* experienced a steady decrease in the number of grid cells with data with potential impacts on the granularity of the field. However, we did not find significant temporal trends in the dispersion statistics of the resulting climatic fields. A reason for this is that in the OI scheme, the information about the spatial variability of the climatic field being reconstructed does not exclusively depend on ground observations, as other methods do, but also on the RCM variance-covariance matrix (**P**), which embeds a physically-based estimation of the spatial variability of the climatic process over the entire domain, including areas sparsely monitored. Since **R** is a diagonal matrix, the spatial correction performed by OI mostly depends on **P** (i.e. on the spatial variability of the climate process extracted from the RCM), which is available for all grid points and reduces the dependency of the resulting field variance on ground observations.

On the other hand, the uncertainty of the estimates $<\boldsymbol{\sigma}^{a}>$, represented on Fig. 9, was very sensitive to the number of stations used, especially for *RH* and *W*. The sharp increment in the density of the observational network for these variables had a strong impact in reducing $<\boldsymbol{\sigma}^{\mathbf{a}}_{RH}>$ and $<\boldsymbol{\sigma}^{\mathbf{a}}_{W}>$. From an algebraic point of view, the increase in the number of grid cells containing data affects the calculation of the gain matrix **K** (Eq. (2)). As **R** decreases, **P** becomes a larger share of the total error variance represented by **K**, informing the updates to increase the amount of correction on the prior estimates (i.e. observations gain influence). When the variance update formula is used to calculate the posterior uncertainty of the estimate ($\mathbf{P}^{+}$), **K** induces a larger reduction in the background uncertainty (**P**).

Similarly, a decrease in the number of observations, such as in the case of *SD*, results in an increase in $<\boldsymbol{\sigma}^{\mathbf{a}}_{SD}>$. This also happens, albeit to a smaller extent, with T_{max} and T_{min}. Nevertheless, the

increment in the number of *RH* and *W* observations was more important than the decrease in the number of observations in these three variables, and the overall uncertainty in the ET_o estimate, $<\sigma^{a}_{ET_o}>$, decreased over the study period.

6. Conclusions

1. The use of an OI scheme blending background RCM data with observational data from a relatively dense network allowed estimating fields of the variables needed to compute fields of FAO-PM ET_o.
2. OI also allowed propagating the initial uncertainty of the data to the OI estimated fields, which were then propagated through the Jacobian of FAO-PM equation to finally get ET_o uncertainty fields.
3. The granularity of the estimated ET_o fields, as measured through their spatial variance, was not affected by changes in the number of stations in the observational network, which were noticeable during the study period. This can be attributed to the physically-coherent information on the spatial structure of the variables provided by the RCM, and contrasts with other methods that rely on observational data alone.
4. The uncertainty of the meteorological variables and therefore of ET_o was, however, sensitive to changes in the number of stations used. In this sense, we found that in our case study the number and spatial distribution of temperature records was adequate for the spatial resolution of our analysis, while a recent increase in the number of air humidity and wind speed stations substantially reduced the uncertainty of computed ET_o. A reduction was found in the number of sunshine duration stations that affected negatively the computation of ET_o.
5. The propagation of uncertainty is a highly relevant issue when constructing meteorological grids but it is often neglected, probably due to difficulties in determining the uncertainty of the original data sources. In this case a number of assumptions were made to quantify the uncertainties of the RCM and observational data used and their consequences were checked and discussed, but other options could be explored.

Acknowledgments

This work has been supported by the research project CGL2014-52135-C3-1-R, financed by the Spanish Ministerio de Economía, Industria y Competitividad (MINECO) and EU-FEDER. M Maneta acknowledges support from the National Science Foundation EPSCoR Cooperative Agreement EPS-1101342, NSF Contracts GSE-1461576 and DGE-1633831, and USDA NIFA contract 2016–67026-25067. The work of M. Tomas-Burguera was supported by the predoctoral FPU program 2013 (Ministerio de Educación, Cultura y Deporte). We wish to thank the Spanish national meteorological service (AEMET) for providing the observational data necessary to carry out this study. We acknowledge the World Climate Research Programme's Working Group on Regional Climate, and the Working Group on Coupled Modelling, former coordinating body of CORDEX and responsible panel for CMIP5. We also thank the DMI climate modelling group for producing and making available HIRHAM model output. We also acknowledge the Earth System Grid Federation infrastructure an international effort led by the U.S. Department of Energy's Program for Climate Model Diagnosis and Intercomparison, the European Network for Earth System Modelling and other partners in the Global Organisation for Earth System Science Portals (GO-ESSP)." We declare that we have no competing interests.

Appendix A. Glossary

$\mathbf{ET_o^a}$:	Reference crop evapotranspiration calculated using meteorological variables estimated by Optimal Interpolation [mm] [dimensions: m]
$\mathbf{ET_o^b}$:	Reference crop evapotranspiration calculated using physically-based climate model data [mm] [dimensions: m]
$\mathbf{H}$:	Mask used to map physically-based climate model data into observations data space [dimensions: $n \times m$]
$\mathbf{I}$:	Identity matrix [dimensions $n \times n$]
$\mathbf{J}_{ET_o}$:	Refers to the Jacobian of $\mathbf{ET_o}$ considering only the partial derivatives of climate variables
$\mathbf{K}$:	Kalman Gain used in the Optimal Interpolation [dimensions: $m \times n$]
m:	Number of physically-based climate grid cells [m = 3930]
n:	Number of grid cells containing at least one weather station. Its value varies for each variable and time step.
$\mathbf{P}_v$:	Error covariance matrix of physically-based climate model variables [dimensions: $m \times m$]
$\mathbf{P}_v^+$:	Posterior error covariance matrix of each climate variable [dimensions: $m \times m$]
$\mathbf{Q}_k$:	Error covariance matrix of the climate variables at the specific location k [dimensions: 5×5]
$\mathbf{R}_v$:	Error covariance matrix of observations. [dimensions: $n \times n$]
$\mathbf{x}_v^a$:	Refers to the Optimal Interpolation climate variable values
$\mathbf{x}_v^b$:	Refers to the Regional Climate Model climate variable values
$\mathbf{x}_v^t$:	Refers to the (unknown) true climate variable values
$\mathbf{y}_v$:	Refers to the observed climate variables values
σ:	Refers to the diagonal positions (the variance) of one of the error covariance matrix
β:	Refers to a fix scaling parameter that controls the magnitude of $\mathbf{R}$
δ:	Refers to the analysis differences between the Optimal Interpolation values and the Regional Climate Model values ($\mathbf{x^a} - \mathbf{x^b}$)
$<\cdot>$:	Refers to the spatial mean of $\cdot$
$\ll\cdot\gg$:	Refers to the spatial standard deviation of $\cdot$
$\bar{\cdot}$:	Refers to the temporal mean of $\cdot$
$\hat{\cdot}$:	Refers to the estimated value of $\cdot$

Appendix B. Uncertainty trends

See Table B.3.

Table B.3
ET_o uncertainty trend.

Month	Tau	2-Sided p value	trend (mm^2/year)
1	−0.50	8.75e−04	−0.08
2	−0.66	1.16e−05	−0.10
3	−0.62	3.00e−05	−0.17
4	−0.48	1.00e−03	−0.12
5	−0.35	0.02	−0.19
6	−0.17	0.24	−0.18
7	−0.63	2.38e−05	−0.46
8	−0.65	1.48e−05	−0.45
9	−0.43	3.60e−03	−0.18
10	−0.45	2.00e−03	−0.14
11	−0.63	2.38e−05	−0.11
12	−0.66	9.12e−06	−0.10

References

Abatzoglou, J.T., 2013. Development of gridded surface meteorological data for ecological applications and modelling. Int. J. Climatol. 33, 121–131. https://doi.org/10.1002/joc.3413.

Allen, R.G., Pereira, L.S., Raes, D., Smith, M., 1998. Crop evapotranspiration – guidelines for computing crop water requirements. FAO Irrigation and Drainage Paper 56, FAO, Rome Italy.

Azorin-Molina, C., Vicente-Serrano, S.M., Sanchez-Lorenzo, A., McVicar, T.R., Morán-Tejeda, E., Revuelto, J., El Kenawy, A., Martín-Hernández, N., Tomas-Burguera, M., 2015. Atmospheric evaporative demand observations, estimates and driving factors in Spain (1961–2011). J. Hydrol. 523, 262–277. https://doi.org/10.1016/j.jhydrol.2015.01.046.

Azorin-Molina, C., Guijarro, J.A., McVicar, T.R., Vicente-Serrano, S.M., Chen, D., Jerez, S., Esírito-Santo, F., 2016. Trends of daily peak wind gusts in Spain and Portugal, 1961–2014. J. Geophys. Res. Atmos. 121, 1059–1078.

Begueŕa, S., Vicente-Serrano, S.M., Tomas-Burguera, M., Maneta, M., 2016. Bias in the variance of gridded data sets leads to misleading conclusions about changes in climate variability. Int. J. Climatol. 36, 3413–3422.

Blaney, H.F., Criddle, W.P., 1950. Determining water requirements in irrigated areas from climatological and irrigation data. USDA (SCS) TP-96, 48.

Brohan, P., Kennedy, J.J., Harris, I., Tett, S.F.B., Jones, P.D., 2006. Uncertainty estimates in regional and global observed temperature changes: a new data set from 1850. J. Geophys. Res. Atmos. 111, D12106. https://doi.org/10.1029/2005JD006548.

Christensen, O.B., Drews, M., Christensen, J.H., Dethloff, K., Ketelsen, K., Hebestadt, I., Rinke, A., 2006. The HIRHAM regional climate model. Version 5. DMI Technical Report 06–17. Available from DMI.

Dee, D.P., Uppala, S.M., Simmons, A.J., Berrisford, P., Poli, P., Kobayashi, S., Andrae, U., Balmaseda, M.A., Balsamo, G., Bauer, P., Bechtold, P., Beljaars, A.C.M., van de Berg, L., Bidlot, J., Bormann, N., Delsol, C., Dragani, R., Fuentes, M., Geer, A.J., Haimberger, L., Healy, S.B., Hersbach, H., Hólm, E.V., Isaksen, L., Kallberg, P., Köhler, M., Matricardi, M., McNally, A.P., Monge-Sanz, B.M., Morcrette, J.-J., Park, B.-K., Peubey, C., de Rosnay, P., Tavolato, C., Thépaut, J.-N., Vitart, F., 2011. The ERA-Interim reanalysis: configuration and performance of the data assimilation system. Q. J. R. Meteor. Soc. 137, 553–597.

Espadafor, M., Lorite, I.J., Gavilán, P., Berengena, J., 2011. An analysis of the tendency of reference evapotranspiration estimates and other climate variables during the last 45 years in Southern Spain. Agric. Water Manage. 98, 1045–1061.

Giorgi, F., Jones, C., Ghassem, R., 2009. Addressing climate information needs at the regional level: the CORDEX framework. World Meteorol. Organiz. Bull. 58 (3), 175–183.

Hargreaves, G.H., Samani, Z.A., 1985. Reference crop evapotranspiration from temperature. Appl. Eng. Agric. 1, 96–99.

Harris, I., Jones, P., Osborn, T., Lister, D., 2014. Updated high-resolution grids of monthly climatic observations – the CRU TS 3.10 dataset. Int. J. Climatol. 34 (3), 623–642.

Hart, Q.J., Brugnach, M., Temesgen, B., Rueda, C., Ustin, S.L., Frame, K., 2009. Daily reference evapotranspiration for California using satellite imagery and weather station measurement interpolation. Civil Eng. Environ. Syst. 26 (1), 19–33.

Haslinger, K., Bartsch, A., 2016. Creating long-term gridded fields of reference evapotranspiration in Alpine terrain based on a recalibrated Hargreaves method. Hydrol. Earth Syst. Sci. 20, 1211–1223.

Hersbach, H., Dee, D., 2016. ERA5 reanalysis is in production. ECMWF Newslett. 147, 7.

Hosseinzadehtalaei, P., Tabari, H., Willems, P., 2016. Quantification of uncertainty in reference evapotranspiration climate change signals in Belgium. Hydrol. Res. 26 (1), 19–33.

Irmak, S., Kabenge, I., Skaggs Mutiibwa, K.E.D., 2012. Trend and magnitude of changes in climate variables and reference evapotranspiration over 116-yr period in the Platter river basin, Central Nebraska-USA. J. Hydrol. 420–421, 228–244.

Ishak, A.M., Bray, M., Remesan, R., Han, D., 2010. Estimating reference evapotranspiration using numerical weather modelling. Hydrol. Process. 24, 3490–3509.

Jiménez, P.A., Dudhia, J., 2012. Improving the representation of resolved and unresolved topographic effects on surface wind in the WRF model. J. Appl. Meteor. Climatol. 51, 300–316.

Kalnay, E., Kanamitsu, E., Kistler, R., Collins, W., Deaven, D., Gandin, L., Iredell, M., Saha, S., White, G., Woollen, J., Zhu, Y., Chelliah, M., Ebisuzaki, W., Higgins, W., Janowiak, J., Mo, K.C., Ropelewski, C., Wang, J., Leetmaa, A., Reynolds, R., Jenne, R., Joseph, D., 1996. The NCEP/NCAR 40-year reanalysis project. Bull. Am. Meteorol. Soc. 77, 437–471.

Kay, A.L., Davies, H.N., 2008. Calculating potential evaporation from climate model data: a source of uncertainty for hydrological climate change inputs. J. Hydrol. 358, 221–239.

Kendall, M.G., 1975. Rank Correlation Methods Griffin. London.

Kerr, A., Tabony, R., 2004. Comparison of sunshine recorded by Campbell-Stokes and automatic sensors. Weather 59 (4), 90–95.

Kingston, D.G., Todd, M.C., Taylor, R.G., Thompson, J.R., Arnell, N.W., 2009. Uncertainty in the estimation of potential evapotranspiration under climate change. Geophys. Res. Lett. 36, L20403. https://doi.org/10.1029/2009GL040267.

Knutti, R., 2010. The end of model democracy? An editorial comment. Clim. Change 102, 395–404.

Kotlarski, S., Keuler, K., Christensen, O.B., Colette, A., Déqué, M., Gobiet, A., Goergen, K., Jacob, D., Lüthi, D., van Meijgaard, E., Nikulin, G., Schär, C., Teichmann, C., Vautard, R., Warrach-Sagi, K., Wulfmeyer, V., 2014. Regional climate modeling on European scales: a joint standard evaluation of the EURO-CORDEX RCM ensemble Geosci. Model Dev. 7, 1297–1333.

Lewis, C.S., Allen, N.L., 2016. Potential Crop Evapotranspiration and Surface Evaporation estimates via a gridded weather forcing dataset. J. Hydrol. 546, 450–463. https://doi.org/10.106/j.jhydrol.2016.11.055.

Lusana, C., 2017. Spatial Interpolation of daily minimum, maximum and mean temperature Norwegian Meteorological Institute Technical Report. 02/2017. ISSN: 2387-4201.

Man, H.B., 1945. Nonparametric tests against trend. Econometrica 13, 245–259.

Mardikis, M.G., Kalivas, D.P., Kollias, V.J., 2005. Comparison of interpolation methods for the prediction of reference evapotranspiration – an application in Greece. Water Resour. Manage. 19 (3), 251–278.

Martins, D.S., Paredes, P., Raziei, T., Pires, C., Cadima, J., Pereira, L.S., 2017. Assessing reference evapotranspiration estimation from reanalysis weather products. An application to the Iberian Peninsula. Int. J. Clim. 37 (5), 2378–2397.

McVicar, T.R., Van Niel, T.G., Li, L., Hutchinson, M.F., Mu, X., Liu, Z., 2007. Spatially distributing monthly reference evapotranspiration and pan evaporation considering topographic influences. J. Hydrol. 338, 196–220.

McVicar, T.R., Roderick, M.L., Donohue, R.J., Van Niel, T.G., 2012. Less bluster ahead? Echohydrological implication of globals trends of terrestrial near-surface wind speeds. Ecohydrology 5 (4), 381–388.

Morice, C.P., Kennedy, J.J., Rayner, N.A., Jones, P.D., 2012. Quantifying uncertainties in global and regional temperature change using an ensemble of observational estimates: the HadCRUT4 data set. J. Geophys. Res. 117, D08101. https://doi.org/10.1029/2011JD017187.

Painter, H.E., 1981. The performance of a Campbell-Stokes sunshine recorder compared with a simultaneous record of the normal incidence irradiance. Meteorol. Mag. 110, 102–109.

Priestley, C.H.B., Taylor, R.J., 1972. On the assessment of the surface heat flux and evaporation using large-scale parameters. Mon. Weather Rev. 100, 81–92.

Prudhomme, C., Williamson, J., 2013. Derivation of RCM-driven potential evapotranspiration for hydrological climate change impact analysis in Great Britain: a comparison of methods and associated uncertainty in future projections. Hydrol. Earth Syst. Sci. 17, 1365–1377.

Reynolds, R.W., Rayner, N.A., Smith, T.M., Stokes, D.C., Wang, W., 2002. An improved in situ and satellite SST analysis for climate. J. Clim. 15, 1609–1625.

Riosalido, R., Vázquez, L., Gordo, A., Jansá, A., 1986. Cierzo: Northwesterly wind along the Ebro Valley as a meso-scale effect induce don the lee of the Pyrenees mountain range: a case study during ALPEX Special Period. Scientific Results of the Alpine Experiment (ALPEX), vol. 2. WMO/TD 108, 943. pp. 565–575.

Robinson, E.L., Blyth, E.M., Clark, D.B., FInch, J., Rudd, A., 2017. Trends in atmospheric evaporative demand in Great Britain using high-resolution meteorological data. Hydrol. Earth Syst. Sci. 21, 1189–1224.

Ruiz-Arias, J.A., Quesada-Ruiz, S., Fernandez, E.F., Gueymard, C.A., 2015. Optimal combination of gridded and ground-observed solar radiation data for regional solar resource assessment. Solar Energy 112, 411–424.

Sanchez-Lorenzo, A., Calbó, J., Wild, M., 2013. Global and diffuse solar radiation in Spain: building a homogeneous dataset and assessing their trends. Global Planet. Change 100, 343–352. https://doi.org/10.1016/j.gloplacha.2012.11.010.

Sheffield, J., Goteti, G., Wood, E.F., 2006. Development of a 50-Year High-Resolution Global Dataset of Meteorological Forcings for Land Surface Modeling. J. Clim. 19, 3088–3111.

Silverman, N.L., Maneta, M.P., 2016. Detectability of change in winter precipitation within mountain landscapes: Spatial patterns and uncertainty. Water Resour. Res. 52, 4301–4320. https://doi.org/10.1002/2014WR016493.

Skamarock, W.C., Klemp, J.B., 2008. A time-split nonhydrostatic atmospheric model for weather research and forecasting applications. J. Comput. Phys. 227 (7), 3465–3485. https://doi.org/10.1016/j.jcp.2007.01.037.

Srivastava, P.K., Han, D., Rico Ramirez, M.A., Islam, T., 2013. Comparative assessment of evapotranspiration derived from NCEP and ECMWF global datasets through Weather Research and Forecasting model. Atmos. Sci. Lett. 14, 118–125. https://doi.org/10.1002/asl2.427.

Strong, C., Khatri, K.B., Kochanski, A.K., Lewis, C.S., Niel Allen, L., 2017. Reference evapotranspiration from coarse-scale and dynamically downscaled data in complex terrain: sensitivity to interpolation and resolution. J. Hydrol. 548, 406–418. https://doi.org/10.1016/j.jhydrol.2017.02.045.

Tomas-Burguera M., Jimenez A., Luna M.Y., Morata A., Vicente-Serrano S.M., González-Hidalgo J.C., Beguería S., 2016. Control de calidad de siete variables del banco nacional de datos de AEMET. In: Olcina Cantos J., Rico Amorós A.M., Moltó Mantero E., (Eds.), Clima, Sociedad, riesgos y ordenación del territorio. Asociación Española de Climatología, Universidad de Alicante, Alicante, Spain, pp. 407–415. https://doi.org/10.14198/XCongresoAECAlicante2016-38.

Tomas-Burguera, M., Vicente-Serrano, S.M., Begueŕa, S., 2017. Accuracy of reference evapotranspiration (ETo) estimates under data scarcity scenarios in the Iberian Peninsula. Agric. Water Manage. 182 (1), 103–116.

Uppala, S.M., Kallberg, P.W., Simmons, A.J., Andrae, U., Bechtold, V.D.C., Fiorino, M., Gibson, J.K., Haseler, J., Hernandez, A., Kelly, G.A., Li, X., Onogi, K., Saarinen, S., Sokka, N., Allan, R.P., Andersson, E., Arpe, K., Balmaseda, M.A., Beljaars, A.C.M., Berg, L.V.D., Bidlot, J., Bormann, N., Caires, S., Chevallier, F., Dethof, A., Dragosavac, M., Fisher, M., Fuentes, M., Hagemann, S., Hölm, E., Hoskins, B.J., Isaksen, L., Janssen, P.A.E.M., Jenne, R., Mcnally, A.P., Mahfouf, J.F., Morcrette, J.J.,

Rayner, Saunders, R.W., Simon, P., Sterl, A., Trenberth, K.E., Untch, A., Vasiljevic, D., Viterbo, P., Woollen, J., 1989. The ERA-40 reanalysis. Q. J. R. Meteor. Soc. 131, 2961–3012. https://doi.org/10.1256/qj.04.176.

Vanderlinden, K., Vicente Giráldez, J., Van Mirvenne, M., 2008. Spatial estimation of reference evapotranspiration in Andalusia, Spain. J. Hydrometeorol. 9 (2), 242–255. https://doi.org/10.1175/2007JHM880.1.

Vicente-Serrano, S.M., Azorin-Molina, C., Sanchez-Lorenzo, A., Revuelto, J., López-Moreno, J.I., González-Hidalgo, J.C., Moran-Tejeda, E., Espejo, F., 2014a. Reference evapotranspiration variability and trends in Spain, 1961–2011. Global Planet. Change 121, 26–40.

Vicente-Serrano, S.M., Azorin-Molina, C., Sanchez-Lorenzo, A., Morán-Tejeda, E., Lorenzo-Lacruz, J., Revuelto, J., López-Moreno, J.I., Espejo, F., 2014b. Temporal evolution of surface humidity in Spain: recent trends and possible physical mechanisms. Clim. Dyn. 42 (9), 2655–2674.

Vicente-Serrano, S.M., Azorin-Molina, C., Sanchez-Lorenzo, A., Revuelto, J., Morán-Tejeda, E., López-Moreno, J.I., Espejo, F., 2014c. Sensitivity of reference evapotranspiration to changes in meteorological parameters in Spain (1961–2011). Water Resour. Res. 50, 8458–8480. https://doi.org/10.1002/2014WR015427.

Wikle, C.K., Berliner, L.M., 2007. A Bayesian tutorial for data assimilation. Physica D 230 (1), 1–16.

Wild, M., Folini, D., Schär, C., Loeb, N., Dutton, E.G., König-Langlo, G., 2013. The global energy balance from a surface perspective. Clim. Dyn. 40 (11), 3107–3134.

World Meteorological Organization, 1989. Calculation of monthly and annual 30-year standard normals WMO-NO. 341. Washington D.C.

World Meteorological Organization, 2003. Manual on the Global Observing System. WMO-NO. 544. Geneva.